https://doi.org/10.5194/egusphere-2026-1953
Preprint. Discussion started: 17 July 2026
© Author(s) 2026. CC BY 4.0 License.

A fast vegetation temperature condition index for operational agricultural drought monitoring at scale.

Darrell Smith[1], Darren Ghent[2], Karen Veal[2], Thomas Dowling[1]

[1]School of Environment, 23 Symonds Street, University of Auckland, Auckland, New Zealand
[2]National Centre for Earth Observation, Department of Physics and Astronomy, University of Leicester, Leicester, United Kingdom.

Correspondence to: Darrell Smith (darrell.smith@outlook.co.nz)

Abstract.

Agricultural adaptation to a changing climate requires frequent, accessible, and reliable information on water availability at spatio-temporal scales relevant to end users. In response to this need, we have developed an approach that evaluates agricultural drought conditions while minimising data and processing costs. This is achieved through an approximation of the land surface temperature–vegetation index (LST-VI) population, which is used in the calculation of the vegetation temperature condition index (VTCI), and the implementation of non-linear edge finding, which more accurately defines the warm and cold boundaries of the population. This 'fast' approach to defining the LST-VI population equally applies to similar vegetation-temperature-based approaches to drought monitoring and is critical to enabling such approaches to be used with higher resolution thermal datasets at scale due to the reduction in run-time and memory requirements it enables. We tested the approach in Taranaki, New Zealand, using the full Moderate Resolution Imaging Spectroradiometer (MODIS) LST and surface reflectance record available through Google Earth Engine. We assessed three vegetation indices and evaluated fast-VTCI outputs against data from 10 ground-based soil moisture monitoring stations. Statistically significant correlations (Pearson's and Spearman's $R=0.21–0.88$, $p<0.01$) demonstrate that fast-VTCI reliably captures spatial and temporal variability in field conditions, achieving performance equivalent to the traditional VTCI method. The strength of the observed correlations varies spatially and temporally for both indices. Overall, fast-VTCI substantially lowers computational costs, enabling efficient, operational drought monitoring across regional to national scales with spatial resolutions that support informed agricultural decision-making.

https://doi.org/10.5194/egusphere-2026-1953
Preprint. Discussion started: 17 July 2026
© Author(s) 2026. CC BY 4.0 License.

1 Introduction

As agricultural drought events become more frequent and severe with climate change, the risks to regional and global food systems are escalating. Drought typically evolves from a precipitation deficit (meteorological drought) and intensifies through elevated evapotranspiration driven by higher temperatures. This leads to reduced soil moisture availability (agricultural drought) and, if prolonged, can diminish streamflow and groundwater reserves (hydrological drought), with cascading socioeconomic effects (West et al., 2019; Liu et al., 2016; Kallis, 2008). The slow onset, varying duration, diffuse boundaries and uneven spatial impacts of drought events challenge both in-situ and remote monitoring. This necessitates drought indices that are tailored to specific user needs, temporal scales and environmental contexts (Wilhite, 2000; Kallis, 2008; Liu et al., 2016).

In Aotearoa New Zealand, drought monitoring remains largely reliant on ground-based approaches. The New Zealand Drought Index (NZDI), the country's primary operational monitoring tool, is derived from approximately 100 automated climate stations (Mol et al., 2017). The NZDI is calculated at each station and then interpolated via a thin-plate smoothing spline method to an approximately 500m grid (Mol et al., 2017). While this provides a consistent national drought signal, the use of interpolation techniques means the index's accuracy is naturally highest near ground station locations and diminishes in areas with sparse coverage or complex terrain. Furthermore, localised effects, such as irrigation or diverse crop types, cannot be adequately captured (Hazaymeh & Hassan, 2016; Ford & Quiring, 2017; Wei et al., 2021). The derived and mapped NZDI is made available to interested parties (such as growers and farmers) as sub-regional averages over time (at cost) or as static national map images (free) (Mol et al., 2017).

Remote sensing-based drought indices offer a scalable solution, decoupling drought monitoring from expensive fixed meteorological stations and enabling consistent assessment across landscapes. Yet, operational implementation at agriculturally relevant spatial resolutions introduces substantial computational and input/output (IO) challenges, particularly for organisations with limited processing infrastructure. This barrier becomes critical as monitoring systems scale from research to operational deployment.

Multispectral, thermal infrared, and microwave sensors enable the generation of grid-based drought indices whose resolution depends on sensor characteristics and processing methods. Passive optical indices (e.g. NDVI) track vegetation condition, while thermal indices (e.g. LST anomalies) reflect surface energy balance changes associated with moisture stress (Hazaymeh & Hassan, 2016). Integrated or composite indices, such as the Vegetation Temperature Condition Index (VTCI), jointly exploit both optical and thermal signals to infer soil moisture and evapotranspiration (Price, 1990; Wang et al., 2001a; Tang et al., 2010; Hazaymeh & Hassan, 2016).

VTCI was first introduced by Price (1990) and later formalised by Wang et al. (2001) and Wan et al. (2004). The index is based on the triangular or trapezoidal shape of an LST and Vegetation Index (VI) population and was proposed to monitor drought conditions at a regional scale (Wang et al., 2001). The widespread adoption of the VTCI and other triangle-based indices stems from their ability to reflect vegetation moisture stress with high accuracy (Wan et al., 2004; Sun et al., 2008;

https://doi.org/10.5194/egusphere-2026-1953
Preprint. Discussion started: 17 July 2026
© Author(s) 2026. CC BY 4.0 License.

Patel et al., 2012). These indices also offer a significant advantage for agricultural applications over conventional in-situ measurements as they reflect surface moisture dynamics rather than soil moisture at a fixed depth (Przeździecki et al., 2023). The LST–VI triangle method underlying VTCI is widely used for regional evapotranspiration estimation (Zhu et al., 2024) and also forms the basis of other indices such as the Temperature Vegetation Dryness Index (TVDI). While both employ the same population space, VTCI normalises to the cold edge and TVDI to the warm edge (Sandholt et al., 2002).

A significant advancement in the LST-VI population space to date has been the introduction of a multiyear approach by Khan et al. (2018), Zhou et al. (2020) and Przeździecki et al. (2023). This approach enables the construction of a more representative and temporally stable LST-VI population. Earlier implementations using this space often relied on a single-day or single-year data, limiting the ability to capture the full range of drought variability within a region over time. Another significant advancement was the introduction of a rules-based edge fitting algorithm by Sun et al. (2008) and Tang et al. (2010). The population's warm and cold edges delineate the limiting boundaries of soil moisture and evaporative fraction, respectively, for any given VI value (Tang et al., 2010; Jiang & Islam, 1999). This development, and later work by Hu et al. (2019), who introduced machine learning techniques, removes significant subjectivity. Combined, these quantitative, multi-annual methods improve reliability and enable consistent drought assessment over time, particularly in regions with high spatial variability in surface roughness and vegetation types.

Despite these advances, several limitations persist. Triangle-based indices assume an inverse relationship between LST and VI, reflecting soil surface heating under water-limited conditions. This assumption does not hold when energy (solar radiation) is the limiting factor, making triangle-based methods only suitable when it is known that negative correlations are in place (Karnieli et al., 2010; Hu et al., 2019). Triangle-based methods also have previously relied on sufficient spatial heterogeneity in vegetation and soil moisture to define the 'warm' and 'cold' edges of the LST-VI population (Holzman et al., 2014); this reliance is resolved in more recent work by Przeździecki et al. (2023) by using long temporal records in the population construction. The widely used linear regression assumption (e.g. Moran et al., 1994; Wan et al., 2004) for defining these edges has also been contested, with evidence indicating that non-linear edges better represent the physical processes involved due to the coupling effect between canopy and soil, affecting surface roughness and thermal dynamics (Hu et al., 2019; Przeździecki et al., 2023; Przeździecki et al., 2020). Finally, index performance is affected at coarser resolutions (Petropoulos et al., 2009) and under dense vegetation, where optical–thermal signals probe only the upper soil layers (Aliyu Kasim et al., 2020).

Although introduced over two decades ago, the VTCI, the TVDI, and the underlying LST–VI triangle method remain important in modern drought research. These methods continue to support the generation of drought analysis products (e.g. Yuan et al., 2023; Przeździecki et al., 2023), the downscaling of satellite-based soil moisture estimates (e.g. Cai et al., 2025), and the development of refined or hybrid indices (e.g. Li et al., 2025). At the same time, advances in satellite remote sensing are driving a shift from moderate-resolution sensors toward the use of higher spatial and temporal resolution datasets for precise agricultural monitoring. A growing suite of open-source, commercial and fused data products now provides daily or near-daily LST observations at spatial resolutions of 20 to 100 m (e.g. Qi et al., 2026; Duan et al., 2025). While these datasets better capture landscape heterogeneity and increase the statistical robustness of LST–vegetation index relationships (Petropoulos et

https://doi.org/10.5194/egusphere-2026-1953
Preprint. Discussion started: 17 July 2026
© Author(s) 2026. CC BY 4.0 License.

al., 2009), they also expose key limitations of traditional VTCI implementations. Specifically, methods that depend on dense per-pixel LST–VI populations become increasingly constrained by input-output overhead and computational burden as observation density increases. For example, processing a single region that generates ~3,800 daily observations at a 1 km resolution would produce ~380,000 observations at 100 m resolution. This represents a 100-fold increase in data volume and processing requirements, which renders these traditional per-pixel approaches computationally prohibitive for operational systems. As a result, there is a growing need for accurate and computationally efficient formulations of triangle-based drought indices that can scale effectively with higher-resolution datasets and larger monitoring areas. This research aims to address these limitations by proposing a computationally efficient and operationally scalable version of the VTCI, named 'fast-VTCI'. To achieve this, we introduce the following key innovations: a statistical approximation of the full LST-VI population space built from as many observations as possible, integration of non-linear edge detection using support vector machine (SVM) regression, and the development of a sensor-independent framework that is applicable across multiple surface temperature and optical VI datasets.

In practice, this new method materially lowers the computational and input/output (I/O) barriers to operational deployment, enabling frequent reprocessing and pixel-scale monitoring in contexts where full per-pixel stacks are impractical or undesirable, such as on cloud computing environments. This enables three practical benefits beyond data volume reduction: i) operational accessibility for agencies and groups with limited compute or storage budgets, ii) faster index refresh that supports near-real-time monitoring and more frequent recalibration, and iii) the capacity to run multi-index or multi-sensor ensembles that would otherwise be precluded by I/O limits. We quantify these benefits using compute and storage benchmarks reported later. We believe that this advance would be of benefit to organisations such as; i) the Food and Agriculture Organization Global Information and Early Warning System on Food and Agriculture (GIEWS) (FAO, 2025), ii) the USGS Famine Early Warning System (FEWS NET) (USGS, 2025) and iii) the Group on Earth Observations Global Agricultural Monitoring (GEO GLAM) crop monitoring programme (GEO, 2025).

In this work, we implement fast-VTCI using the Google Earth Engine (GEE) platform. We evaluate the new method over an agriculturally critical region in New Zealand using the full record of the MODIS LST and Surface Reflectance datasets available on GEE. Testing the algorithm in a variable climate, such as New Zealand, provides a robust test of the algorithm's sensitivity and generality. Three unique vegetation indices and both linear and polynomial edges are used to generate fast-VTCI results. Each index-edge result set is then tested against in situ soil moisture observations spanning up to 13 years, from an independent network of ten soil moisture monitoring stations. Validation results are compared against equivalent statistics derived from a traditional VTCI implementation.

https://doi.org/10.5194/egusphere-2026-1953
Preprint. Discussion started: 17 July 2026
© Author(s) 2026. CC BY 4.0 License.

2. Materials and methods

2.1 Study region

This research assesses drought conditions in the Taranaki region on the west coast of Aotearoa New Zealand's North Island. Taranaki Maunga lies near the region's centre and rises 2518 m above mean sea level (Chappell, 2014). The volcanic soils in the region are both highly fertile and free draining, making them particularly ideal for pastoral farming (Chappell, 2014). The volcano's influence extends beyond the region's soils, significantly impacting the local topography and climate dynamics (Hockings, 1982). The region encompasses 723,610 hectares, with approximately 50% of this area dedicated to primary agricultural and horticultural production (TRC, 2024; TRC, 2022). Fig. 1 below shows the location and land cover of the monitoring region.

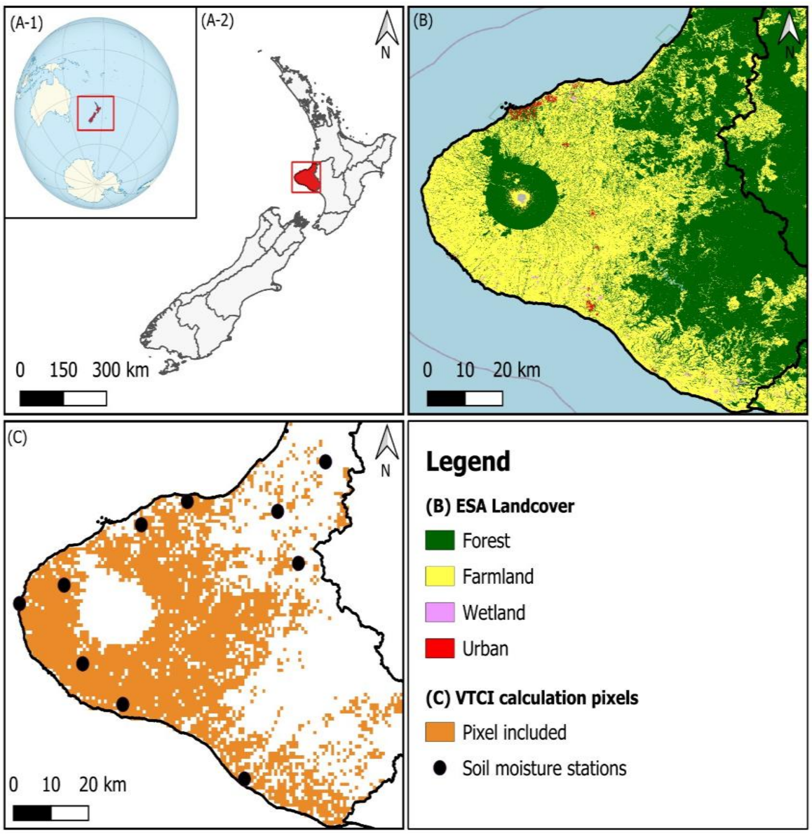

Figure 1. (A) Taranaki location (A-2, red box) in the context of New Zealand's location (A-1, red box). (B) Taranaki Landcover Classification. (C) Soil moisture monitoring stations and valid agricultural VTCI calculation pixels, LCC & DEM filtering (orange). Landcover data from ESA WorldCover v200 (Zanaga et al., 2021), NZ administrative boundaries from StatsNZ (2025) and the world map from WikiMedia Commons (2025).

Principal crops in the region include perennial exotic grasslands (~51% of total land cover in 2019), which support intensive pastoral grazing; other croplands make up only 1% of land cover. These crops include maize, fodder beet and chicory (LAWA, 2018). Pasture growth in the region typically peaks in October, remaining high through late spring and early summer before decreasing in late summer and autumn (DairyNZ, 2020).

New Zealand's climate is predominantly shaped by its oceanic surroundings, which influence air circulation and seasonality, and by its mountainous terrain, which disrupts atmospheric flows and creates rain shadow effects (Caloiero, 2017). The effects of climate change in New Zealand are anticipated to intensify the frequency and severity of droughts (MfE & Stats NZ, 2020).

2.2 Data

All data used to generate fast-VTCI results were sourced from the Google Earth Engine (GEE) Data Catalog. The primary input datasets were obtained from the MODIS Terra sensor, which was selected for its long, internally consistent observational record extending from February 2000, and its extensive use in previous VTCI studies (e.g. Wan et al., 2004; Patel et al., 2012; Khan et al., 2018). These sensor characteristics allow the performance of the fast-VTCI approximation to be evaluated across a wide range of climatic conditions and directly compared with previous VTCI implementations, while minimising uncertainty arising from data fusion methods. Establishing the accuracy, stability, and computational advantages of fast-VTCI using MODIS is a necessary step to establish proof-of-concept prior to its transfer and operational application to higher-resolution thermal datasets.

Land surface temperature inputs were derived from the MOD11A1.061 Terra Land Surface Temperature and Emissivity product, which provides daily observations at 1 km spatial resolution on a 1200 × 1200 km global grid (Wan et al., 2021). Vegetation indices were calculated using the MOD09GA.061 Terra Surface Reflectance product, which also provides daily coverage but at a finer spatial resolution of 500 m (Vermote and Wolfe, 2021). In addition to the core LST and SR data, three other datasets are used to support the analysis: i) a digital elevation model (DEM), ii) a landcover class map (LCC) and 2m daily air temperature (T2m). Static DEMs and LCC maps were used in this work after considering the coarse spatial resolution of the core LST data, reprojected and reduced VI data, and limited local topological and landcover changes over the study period in this region. Copernicus data products were used for the DEM and LCC map, specifically the Copernicus Global Land Cover Layer: CGLS-LC100 Collection 3 – 2019 LCC map (Buchhorn et al., 2020) and Copernicus DEM GLO-30: Global 30m Digital Elevation Model (Fahrland et al., 2022). For the T2m dataset used in surface temperature outlier detection, the ERA5 land dataset from ECMWF was selected. This dataset provides hourly air temperature data on a ~9 km grid and is publicly available with a five-day delay (Muñoz-Sabater et al., 2021).

The Taranaki Regional Council provided soil moisture data for ten regional sampling sites (TRC, 2026) within the study region (see Fig. 1). Soil moisture measurements were obtained from each site using a single-sloping Aquaflex sensor. The Aquaflex sensor records the dielectric constant of the soil along its full 3m length (Aquaflex, n.d.). These readings are then converted into measurements of average volumetric soil moisture (measured in percentages). These sensors were installed according to the manufacturer's recommendations for pasture monitoring. This means the sensor is installed on a slope to assess soil moisture over the entire pasture root zone (typically around 0.5m) (Aquaflex, n.d.). Validation work by Plauborg et al. (2005)

https://doi.org/10.5194/egusphere-2026-1953
Preprint. Discussion started: 17 July 2026
© Author(s) 2026. CC BY 4.0 License.

and later KC et al. (2021) demonstrates that the Aquaflex sensors are effective for agricultural soil moisture monitoring in New Zealand. Soil moisture daily averages were calculated for each site.

NZDI district averages for New Plymouth, Stratford and South Taranaki were sourced from NIWA's NZDI webpage (NIWA, 2026). Data from 2011 onwards was compared against the provided in-situ soil moisture data and calculated fast-VTCI results. Lower level, interpolated cell, NZDI data is only available on a commercial (paid-for) basis and, therefore, was not used in this study.

2.3 fast-VTCI

The traditional VTCI drought index is calculated by comparing an observed VI-LST pair to the historical minimum and maximum LSTs associated with a given VI value in a region. Specifically, it measures the ratio between the difference of the observed LST and the regional minimum LST for the corresponding VI value (Figure 2). This ratio (index) is a measure of crop thermal condition. VTCI is formally defined as (from Wan et al., 2004) eq. 1):

$$VTCI = \frac{LST_{VI_{i,max}} - LST_{VI_i}}{LST_{VI_{i,max}} - LST_{VI_{i,min}}} \quad (eq.1)$$

Where $LST_{VIi,max} = b_w + a_w \cdot VI_i$ and $LST_{VIi,min} = b_c + a_c \cdot VI_i$, where b_w, a_w and b_c, a_c are the linear coefficients of the warm and cold edges derived from the LST-VI space. The subscript 'i' denotes a specific pixel observation within the study area. Explanation of terms provided in Fig 2.

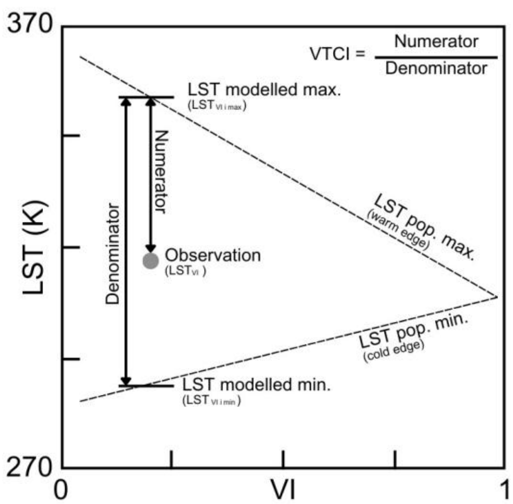

Figure 2. Theoretical model of the LST-VI triangle space and derivation of VTCI. Modified from Wan et al. (2004). LST = land surface temperature. VI = Vegetation index. Pop. = population of the LST-VI space for the given observation region and time, driven by the LST-VI multi-annual database and found with linear regression of the warm and cold edges. The notation in brackets indicates the values input to the VTCI equation for the given observation when deriving the daily VTCI.

https://doi.org/10.5194/egusphere-2026-1953
Preprint. Discussion started: 17 July 2026
© Author(s) 2026. CC BY 4.0 License.

The 'fast' element of fast-VTCI is achieved using a daily approximation of the LST-VI space when building the LST-VI multi-annual regional database (see section 2.4.3). Replacing the full per-pixel LST-VI population with an approximate representation is a simple but highly effective modification that yields a substantial reduction in processing time during warm and cold edge identification. Because edge detection is performed each time VTCI is computed (i.e. daily when using MODIS data), this change markedly lowers the dominant computational costs of the workflow. Furthermore, the resulting LST-VI databases are significantly reduced in size, making storing large and long-term derived records much more feasible for a wide range of stakeholders.

Calculating and validating the fast-VTCI for the Taranaki region is split into several key steps, as shown in Fig. 3 below. To build a robust LST-VI space that quantitatively reflects soil and vegetation conditions over the entire period, the full MODIS data record available on the GEE Data Catalog is used. This space is then evaluated for warm and cold edges using a support vector regression (SVR) model with a polynomial kernel. Prior work has shown that the VTCI is only effective as a drought monitoring index in the warm season, where LST and NDVI are negatively correlated (Karnieli et al., 2010; Hu et al., 2019). This work uses MODIS LST and SR images from between October 01 and March 31 for each year between 2000 and 2024. This period covers Taranaki's summer (Dec-Feb) and aligns well with the peak pasture growth season, making it agriculturally relevant.

https://doi.org/10.5194/egusphere-2026-1953
Preprint. Discussion started: 17 July 2026
© Author(s) 2026. CC BY 4.0 License.

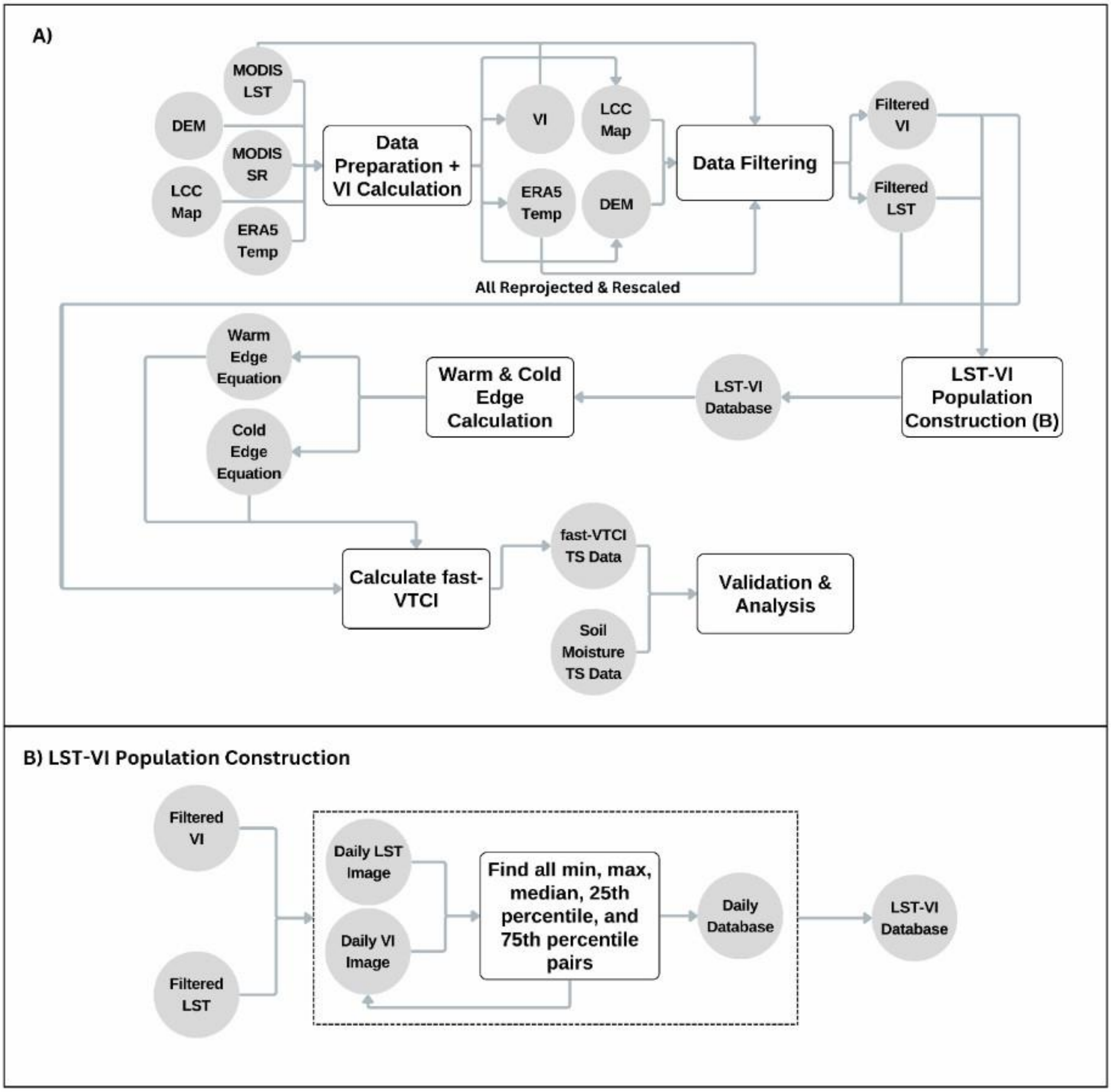

210 **Figure 3: Panel (A): Overview of the fast-VTCI implementation; circles indicate datasets, whilst rectangles are for operations. Panel (B): Detail of the LST-VI space approximation. The dashed-line box encloses a loop performed over every LST-VI array input to the database. When the workflow is implemented in an operational framework, the 'LST-VI Population Construction' step becomes an append of the summary statistics for the given array to the existing LST-VI database, and this updated database is then used to generate new warm and cold edges and fast-VTCI results.**

https://doi.org/10.5194/egusphere-2026-1953
Preprint. Discussion started: 17 July 2026
© Author(s) 2026. CC BY 4.0 License.

2.3.1 Data preparation and VI calculation

All fast-VTCI datasets are reprojected and rescaled to the same projection and scale as the MODIS LST dataset using a bilinear resampling method. In this work, we trialled the NDVI, Soil Adjusted Vegetation Index (SAVI), and Enhanced Vegetation Index (EVI) to calculate fast-VTCI (see Table 1 below).

Table 1: Vegetation indices, equations and parameters used in testing fast-VTCI

Vegetation Index	Equation	Parameters
NDVI (Rouse et al., 1973)	$\boldsymbol{NDVI = \frac{NIR - Red}{NIR + Red}}$	NIR= Near-infrared band RED = Red band
SAVI (Huete, 1988)	$\boldsymbol{SAVI = (1 + L)\frac{(NIR - Red)}{(NIR + Red + L)}}$	L = soil adjustment factor. The soil adjustment factor (L) is set to 0.5 to calculate the SAVI based on Huete (1988).
EVI (Huete et al., 1999; Didan & Munoz, 2019)	$\boldsymbol{EVI = G\frac{(NIR - Red)}{(NIR + C_1Red - C_2Blue + L)}}$	Blue = Blue band, L = canopy background adjustment factor, C1 and C2 = correction factors for aerosol scattering and absorption, and G = gain or scaling factor. G is set to 2.5, C1 to 6, C2 to 7.5 and L to 1.0 per the most recent MODIS VI guidance (Didan & Munoz, 2019).

2.3.2 Pre-database ingestion VI & LST data filtering

As each daily array of MODIS LST and VI values is ingested into the LST-VI database, they are filtered to eliminate sources of error and remove gross outliers. The first pixel-wise filter to be applied uses the LCC map to reduce outliers within the LST-VI space by removing all parts of the region except agricultural areas (landcover classes 30 and 40). The removal of non-agricultural areas (such as snow, surface water, urban and forest areas) is necessary for a long time series due to the outliers commonly generated by such surfaces being inherently more frequent within a multi-annual database as compared to the more limited time series and regional extents used in previous works. To correct regional errors in the LCC map, a DEM filtering step is applied to mask all pixels with an elevation greater than 600m.

The second filter applied uses air temperature at 2m above the land surface (T2m) to help reduce the impact of residual cloud contamination. Specifically, we use the maximum ERA5-Land T2m value across the region at 04:00 local time, which typically

https://doi.org/10.5194/egusphere-2026-1953
Preprint. Discussion started: 17 July 2026
© Author(s) 2026. CC BY 4.0 License.

corresponds to the daily minimum in the diurnal temperature cycle (Hooker et al., 2018). Any LST pixel with a value lower than this regional threshold is likely affected by cloud cover and is therefore excluded (Shi et al., 2016; Dowling et al., 2022). A regional rather than pixel-wise threshold is applied to mitigate the ERA-5 dataset limitations in coastal portions of the study region. The effect of this is to put in place a lower-bounds threshold that identifies very cold outliers but does so in a way that has more physical justification and is related to the area under observation than if a simple lower threshold were used (Dowling et al., 2022). We note that this only holds under certain conditions (clear nights, sufficiently emissive surfaces, low water vapour, etc.), and hence the conservative value is set in order to avoid clearing pixels that cannot meet these conditions.

The last filter applied is a simple range filter to both LST and VI values to remove gross errors not otherwise caught by the prior steps. Each of the three VIs is considered valid between 0.01 and 1.00, with LST considered between 275 and 360 K. A final filtering step compares the VI and LST images for each day and masks any remaining pixels where corresponding data is unavailable.

We justify removing VI values outside of the 0.01-1.0 range due to the likelihood of their cause being the reflection of non-vegetative green light over bare soil and snow surfaces or atmospheric aerosol noise (Huete & Liu, 1994). Three considerations drive the LST threshold range: (i) failures in the LST product cloud filtering, (ii) unflagged snow and (iii) agriculturally relevant temperatures. Given these three elements and the fact that frozen surfaces are not agriculturally relevant for crop growth (Trnka *et al.*, 2010), we set a lower bound that removes pixels below 275 K. The upper bound of 360 K is not set to limit the LST-NDVI space to crop-specific transpiration ranges but to remove unfeasibly high LST values missed in the native product QA flagging.

The application of these filters means that we may miss some of the true LST-VI range within a day, which is against the recommendations of Tang et al. (2010). However, these steps are vital to reduce outliers that would otherwise distort the overall shape of the warm and cold edge boundaries and prevent the proper functioning of the edge-finding algorithm. Robust outlier removal is particularly important in the fast-VTCI approach, given that the LST-VI space edge detection relies on assessing maximum and minimum values within the intervals. If true outliers are not removed, they will distort the approximated space more significantly.

2.3.3 LST-VI population space approximation

The key innovation in this work is the approximation of the LST-VI population space, which is essential due to the volume of data. For the study region alone, at MODIS-resolution, considering all LST-VI pairs can result in as many as 3,817 value sets on any given day, post-filtering.

Whilst this data load is feasible in a high-performance computing environment, it is neither desirable nor necessary. Using the full dataset leads to excessive processing times for a workflow that must be carried out for multiple locations, at least once every 24 hours, to run as an effective operational system. Therefore, a faster calculation of VTCI is necessary for the downstream agricultural industry and other stakeholders to adopt the metric.

https://doi.org/10.5194/egusphere-2026-1953
Preprint. Discussion started: 17 July 2026
© Author(s) 2026. CC BY 4.0 License.

We solve this through the observation that VTCI needs only two elements of all the data present in an LST-VI space in order to operate: 1) the edges (maximum and minimum) of the population distribution of LST for any given VI value in order to calculate VTCI, and 2) some estimation of the most common LST values for a given VI value (median, 25th and 75th percentile), in order to enable edge detection, outlier identification and filtering. It is therefore hypothesised that we can approximate the LST-VI population space with daily LST-VI population summary statistics and fulfil both needs.

The approximation is carried out by sampling each regional set of VI and LST images for the maximum, minimum, 25th percentile, 75th percentile and median values. VI and LST are evaluated separately for each summary statistic, and the unique LST-VI pairs (and VI-LST pairs) are found (minimum 10 unique pairs per image set). The separate evaluation of VI (P_{VI}) and LST (P_{LST}) is done to build a robust population description in both axes of the LST-VI space. The 25th and 75th percentiles are used in addition to the median to represent better populations that are not normally distributed. Where a summary LST / VI value (e.g., 305K or 0.5) occurs in more than 1 pixel in an image, all relevant LST-VI / VI-LST pairs from the image are saved. Where a calculated statistical value (median, 25th percentile, 75th percentile) does not exist in a single pixel in the daily image, the closest pixel value is used. Equations 2, 3 and 4 describe the daily approximation (P_{daily}) of the LST-VI population space:

$$P_{daily} = \begin{bmatrix} P_{LST} \\ P_{VI} \end{bmatrix} \; (eq. 2)$$

Where:

$$P_{LST} = \begin{bmatrix} max(LST) \;\; VI_{max(LST)} \\ min\;(LST) \;\; VI_{min(LST)} \\ median(LST) \;\; VI_{mediqn(LST)} \\ P_{25}(LST) \; VI_{P_{25}(LST)} \\ P_{75}(LST) \; VI_{P_{75}(LST)} \end{bmatrix} \; (eq. 3)$$

$max(LST)$, $min(LST)$, $median(LST)$, $P_{25}(LST)$ and $P_{75}(LST)$ are the maximum, minimum, median, 25th percentile and 75th percentile of the LST array. $VI_{max(LST)}$, $VI_{min(LST)}$, $VI_{median(LST)}$, $VI_{P_{25}(LST)}$ and $VI_{P_{75}(LST)}$ are the values in the VI image where the corresponding values in the LST array occur.

Similarly:

$$P_{VI} = \begin{bmatrix} max(VI) \;\; LST_{max(VI)} \\ min(VI) \;\; LST_{min(VI)} \\ median\;(VI) \;\; LST_{median(VI)} \\ P_{25}(VI) \; LST_{P_{25}(VI)} \\ p_{75}(VI) \; LST_{P_{75}(VI)} \end{bmatrix} \; (eq. 4)$$

https://doi.org/10.5194/egusphere-2026-1953
Preprint. Discussion started: 17 July 2026
© Author(s) 2026. CC BY 4.0 License.

Where $max\ (VI)$, $min(VI)$, $median(VI)$, $P_{25}(VI)$ and $P_{75}(VI)$ are the maximum, minimum, median, 25th percentile and 75th percentile of the VI array. $LST_{max(VI)}$, $LST_{min(VI)}$, $LST_{median(VI)}$, $LST_{P_{25}(VI)}$ and $LST_{P_{75}(VI)}$ are the values in the LST array that correspond to the values in the VI array.

This statistical approximation preserves the defining characteristics of the LST–VI feature space while substantially reducing storage and processing demands. Because traditional VTCI requires only the temperature range for each vegetation index to define the cold and warm edges of the triangle, retaining daily maxima and minima captures the key boundaries. The inclusion of the median and interquartile percentiles (25th and 75th) provides a robust description of the distribution's central tendency and spread, improving outlier rejection and reducing sensitivity to single-pixel noise and residual cloud contamination. Collectively, these summary statistics are conceptually equivalent to constructing the full LST–VI population but replace O(N) storage and computation with O(k) daily summary statistics, where k is constant, yielding reductions in data volume by several orders of magnitude. This reduction in data volume enables rapid data (re)processing with comparative ease. Importantly, this approximation maintains the conceptual integrity of traditional VTCI and related triangle-based drought indices by explicitly preserving the relevant data required for edge detection and robust outlier handling. The LST–VI population is reconstructed from these daily extrema and percentile statistics (Eqs. 2–4), such that limiting boundary behaviour and distributional structure are retained. In this sense, the approach represents a controlled, lossy compression that directly preserves the original VTCI definition.

2.3.4 Edge finding

Figure 4 illustrates the implementation of the modified Tang et al. (2010) edge-finding algorithm with Hu *et al.*'s (2019) additional outlier removal steps. We applied the edge-finding algorithm to both the warm and cold edges (rather than just the warm edge) as we found the lower edge of the LST-VI space to need defining as per the warm edge, as opposed to a static minimum edge used in prior works (e.g. Tang *et al*. 2010). The edge-finding algorithm works by searching for the maximum or minimum LST values (max/min) within 20 evenly dispersed intervals along the full x-axis (VI) (an interval occurs each 0.05 along the axis). Hu et al.'s (2019) and Tang et al.'s (2010) outlier removal filters are applied to the data before regression, to find the warm or cold edge, which is performed upon these max/min values. It is noted that further advancements in edge finding can be found in Cai et al. (2025). For the purposes of this work, we apply the earlier methods to enable direct comparison with work that is focused on drought detection.

For the purposes of outlier removal, the 20 intervals are further divided into ten sub-intervals (200 total sub-intervals). The Hu *et al*. (2019) filter is the first to be applied, and it takes the form of a one-pass test where any observation within a sub-interval greater than three standard deviations above or below the mean of the given subinterval is removed. Secondly, we apply the Tang et al. (2010) filter. Initially, this was a two-step filter with dual removal loops. However, we do not use the second removal loop as it was found that the approximation of an LST-VI space in combination with a non-linear edge removes the need for it. In the remaining Tang et al. (2010) first step, the entire sub-interval is removed from the interval if the

https://doi.org/10.5194/egusphere-2026-1953
Preprint. Discussion started: 17 July 2026
© Author(s) 2026. CC BY 4.0 License.

maximum/minimum of that sub-interval is more than one standard deviation away from the mean of all the sub-intervals within the given interval. The process is repeated until the condition is satisfied.

The edge-finding method's final modification is introducing a non-linear edge definition. Przeździecki et al. (2023) explored this approach in their work on forest area soil moisture estimation and found it to be more effective than the prior linear approaches. The reader is directed to their work for more details on the reasoning behind this improvement. The non-linear edges are found using the support vector regression (SVR) model of SciKitLearn by Pedregosa et al. (2011).

Once outlier removal has occurred and the final trained model is found, the model is passed to the VTCI calculation script as an equation, returning the min/max LST of any VI value. Every instance of SVR model training uses a polynomial kernel with 5 degrees of freedom, C = 100, epsilon = 0.1, coef0 = 1, with the gamma set to automatic. These parameters were settled upon as they best describe the edges while avoiding overfitting. The use of SVR in combination with the approximation-based edge-point finding is an efficient solution that produces well-described edges in a fraction of the time taken by the method as implemented by Tang et al. (2010) and Zhou et al. (2020). Linear edges were also generated using the same outlier removal steps and input data for comparison. Only one set (warm and cold) of polynomial and linear edges were calculated for each index using the full LST-VI database to generate the results presented in this paper.

https://doi.org/10.5194/egusphere-2026-1953
Preprint. Discussion started: 17 July 2026
© Author(s) 2026. CC BY 4.0 License.

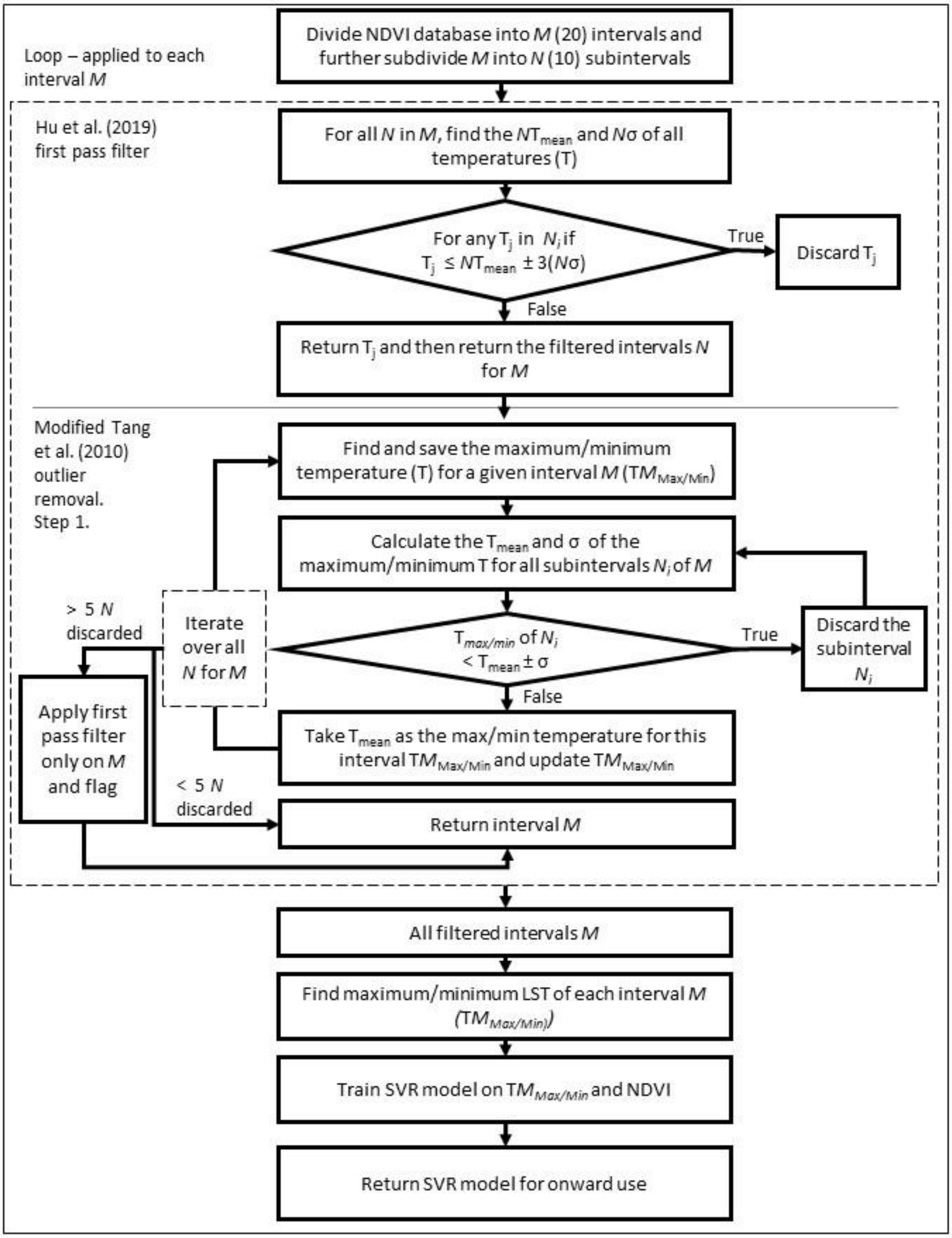

335 **Figure 4: The edge finding algorithm implemented in this work and applied to the search for both warm and cold edges of the LST-VI space. Solid rectangles indicate a computational step, dashed rectangles a loop over a population of LST values and diamonds a**

https://doi.org/10.5194/egusphere-2026-1953
Preprint. Discussion started: 17 July 2026
© Author(s) 2026. CC BY 4.0 License.

threshold decision. M are the primary interval divisions, and N are the subintervals of each interval M. T is a satellite-derived LST value, σ is the standard deviation, RMSE is the root mean square error and |Δ| is the absolute difference. Subscript i denotes an individual subinterval within an interval, and subscript j denotes an individual temperature within an LST population. SVR = support vector regression, used here with a polynomial kernel and 5 degrees of freedom.

A limitation of the VTCI method is that it can, in theory, return values outside the index range of 0-1 when surface temperatures within a scene fall outside the space defined by the warm and cold edges. Hence, we limit VTCI to only assess conditions that occur within the parameters of the data used to build the LST-VI space. By using as long a data record as possible and, when running operationally, updating the LST-VI space and subsequent edge definitions with each new image set, we extend the range of conditions under which VTCI can be calculated. The need to update the LST-VI database and recalculate the edges with every new data input in an operational drought monitoring system is the primary driver for implementing LST-VI space approximation and therefore 'fast-VTCI'.

2.3.5 fast-VTCI calculation and validation

Both sets of warm and cold polynomial and linear edges were returned as the edge function equations. These equations were used to calculate fast-VTCI for all relevant pixels in the region (see Fig. 1) across the entire time series for each VI. For comparison, results were also produced using the traditional VTCI method for the SAVI index using both linear and polynomial edges. These VTCI results were then sampled from 2011 to 2023 for ten single pixels corresponding to the location of each in-situ soil moisture station. This narrower validation period was selected as robust soil moisture data records do not extend prior to 01/01/2011 in the study region. For each monitoring site, VTCI results were joined to corresponding soil moisture measurements using the observation date. A 10-day and a 30-day rolling mean were then calculated for both the VTCI and soil moisture values, thereby smoothing short-term variability, minimising the impact of missing VTCI observations due to cloud cover, and enabling clearer identification of temporal patterns. Records were filtered to exclude dates where the 10-day rolling mean could not be computed due to data gaps. The cleaned data from all sites and index-edge combinations were compiled into a single dataset, with each record representing a site observation for which complete rolling-mean data were available.

Using this consolidated dataset, validation metrics were calculated for the full study period across all sites. Metrics were calculated using the calculated 10-day rolling mean VTCI and soil moisture values unless otherwise mentioned. Validation analyses were also completed at the site level using all years of data from each soil moisture station, at the hydrological year level using all site data for each summer period, and at the site-year level to assess summer-specific relationships at individual locations.

Comparisons were also made to the relevant NZDI data using the same date-based join. The NZDI values were normalised to between 0 (extreme drought) and 1 (normal conditions) to enable unitless and more direct comparison with the fast-VTCI results and soil moisture datasets.

https://doi.org/10.5194/egusphere-2026-1953
Preprint. Discussion started: 17 July 2026
© Author(s) 2026. CC BY 4.0 License.

3. Results

3.1 LST-VI population behaviour and edge fitting performance

LST-VI population scatterplots (see Fig 10) were created using NDVI, SAVI and EVI, with linear and polynomial edges fitted to each population. Each index generated a distinct distribution and therefore warm and cold edges. NDVI showed the highest density of observations at high VI values (most concentrated around ~0.8). By contrast, SAVI and EVI peaked around 0.6. Differences between indices were more pronounced along the VI axis than the LST axis.

The coefficient of determination (R^2) was used to evaluate how well fitted edges represent the upper (warm) and lower (cold) bounds of the LST–VI space. R^2 was calculated from the maximum (warm edge) and minimum (cold edge) data points for each of the 20 intervals in the edge calculation script (section 2.4.5; supplementary materials). Table 2 shows that polynomial edges consistently outperform linear edges in capturing the LST–VI boundary structure, producing substantially higher R^2 values across all vegetation indices. Differences between traditional VTCI and fast-VTCI edges were minimal, with the SAVI exhibiting the highest reliability overall. Cold-edge fits for NDVI and EVI performed notably worse than warm edges, though polynomial edges still exceeded linear fits in all cases. These results highlight the limitations of linear edges in representing the boundaries of the LST–VI space and underscore the value of polynomial regression for robust edge construction.

Table 2: R^2 per edge fitted, for each combination of edge type, vegetation index and edge fitting method.

	Polynomial Edges		***Linear Edges***	
Index	**Warm Edge – R^2**	**Cold Edge – R^2**	**Warm Edge – R^2**	**Cold Edge – R^2**
SAVI (Traditional VTCI)	0.93	0.81	0.13	0.64
SAVI (fast-VTCI)	0.88	0.89	0.14	0.61
NDVI (fast-VTCI)	0.82	0.49	0.11	0.07
EVI (fast-VTCI)	0.93	0.43	-0.12	-0.04

3.2 Validation with in-situ soil moisture data

Each set of VTCI results was validated against in-situ soil moisture observations using linear regression analysis (see section 2.3.5). This validation aimed to quantify the strength of the relationship between VTCI and on-the-ground soil moisture conditions. Table 3 summarises the Pearson correlation coefficients obtained for each index and edge-fitting combination. These are presented for the complete dataset, as well as for selected sites and time periods. Full validation results are provided in the supplementary material.

https://doi.org/10.5194/egusphere-2026-1953
Preprint. Discussion started: 17 July 2026
© Author(s) 2026. CC BY 4.0 License.

Table 3: Summary validation table showing all index /edge sets.

Pearsons Correlation (r)	Edge-Index Sets							
	Traditional VTCI		fast-VTCI					
	SAVI Poly	SAVI Linear	SAVI Poly	SAVI Linear	NDVI Poly	NDVI Linear	EVI Poly	EVI Linear
Overall (All data)	0.45	0.44	0.44	0.45	0.44	0.48	0.44	0.44
Kaūpokonui Site Only	0.65	0.64	0.64	0.64	0.64	0.70	0.63	0.63
2017/18 Year Only (All Sites)	0.58	0.58	0.56	0.57	0.57	0.61	0.59	0.59
Pātea Site - 2017/18 (Summer Only)	0.88	0.86	0.84	0.83	0.83	0.86	0.88	0.84

These results indicate that all index-edge sets demonstrated statistically significant relationships with soil moisture, with p-values consistently below 0.01. Across the full dataset, Pearson correlation coefficients ranged from 0.44 to 0.48, with NDVI-Linear achieving the highest correlation. At the Kaūpokonui site, the relationships were stronger, with all edge-index combinations exceeding 0.6. Temporal validation for the 2017/18 year across all sites showed similar correlations. The strongest relationships were observed at the Pātea site during the 2017/18 summer, where correlations exceeded 0.80 for all configurations. Across all sites and time periods presented above, the fast-VTCI results produced correlations that were almost indistinguishable from those of traditional VTCI in the SAVI Polynomial and Linear configurations.

Based on interpretations from the LST-VI scatterplots, edge fitting and the above validation results, the SAVI-Polynomial edge-index set is selected to explore the temporal and spatial differences in correlations. Similar trends are evident in the EVI and NDVI linear and polynomial edge-index sets. Table 4 provides a breakdown of the total count of smoothed observations, the actual count of VTCI observations, Spearman and Pearson correlations, and the Root Mean Square Error (RMSE), offering insight into the performance of the fast-VTCI and traditional VTCI results at each site. RMSE is a measure of the average magnitude of prediction errors, indicating how closely the estimated VTCI values align with observed soil moisture values.

Significant spatial variation in the strength of relationships between fast-VTCI results and soil moisture data is observed (Table 4). Sites such as Kaūpokonui, Motunui, and Waiwhakaiho showed the strongest relationships, with Spearman correlation of 0.67, 0.63, and 0.62, respectively. These sites also had high Pearson correlations (ranging from 0.60 to 0.64) and lower RMSE values (20% to 22%). In contrast, sites such as Kōtare and Pohokura exhibited comparatively weaker correlations (Spearman = 0.49 and 0.44, Pearson = 0.46 and 0.42). At Kapoaiaia and Stony, moderate correlations exist (Spearman = 0.55); however, these sites also experience higher RMSE values (35% and 34%). Across all sites, the results presented in Table 4 show that traditional VTCI delivers correlations and RMSE values that very closely match those derived from the fast-VTCI method.

It is noted that the number of valid VTCI observations, and consequently the number of smoothed observations, is generally higher for traditional VTCI than for fast-VTCI. This reflects differences in the calculated edges stemming from the underlying

https://doi.org/10.5194/egusphere-2026-1953
Preprint. Discussion started: 17 July 2026
© Author(s) 2026. CC BY 4.0 License.

LST–VI databases: the separation between the traditional VTCI warm and cold edges is, on average, 9% larger than that of fast-VTCI (see Supplementary Materials). The wider population space between edges allows some additional pixels to have VTCI calculated, whereas these same pixels are excluded from fast-VTCI calculation as outliers because either one or both LST/SAVI values fall outside the more tightly constrained edges (see Section 2.3).

Table 4: Site-wise validation for all available data using both the fast-VTCI method (bolded) and traditional VTCI method (italics) with an SAVI-Polynomial index-edge set (all p-values <0.01).

Site	n smoothed observations		n VTCI observations		Spearman correlation		Pearson correlation		RMSE (%)	
Kapoaiaia	**2184**	*2263*	**701**	*1034*	**0.55**	*0.58*	**0.57**	*0.60*	**35**	*32*
Kaūpokonui	**2286**	*2286*	**863**	*873*	**0.67**	*0.68*	**0.64**	*0.65*	**22**	*22*
Kōtare	**1919**	*2069*	**474**	*685*	**0.49**	*0.51*	**0.46**	*0.49*	**21**	*18*
Motunui	**1948**	*1951*	**818**	*826*	**0.63**	*0.64*	**0.60**	*0.61*	**20**	*20*
Pātea	**1420**	*1420*	**645**	*652*	**0.47**	*0.48*	**0.48**	*0.48*	**23**	*24*
Pohokura	**1651**	*1651*	**535**	*536*	**0.44**	*0.44*	**0.42**	*0.42*	**18**	*18*
Stony	**1405**	*1405*	**440**	*443*	**0.55**	*0.55*	**0.54**	*0.54*	**34**	*35*
Taungatara	**1878**	*1879*	**614**	*619*	**0.59**	*0.60*	**0.58**	*0.59*	**20**	*20*
Urutī	**2169**	*2172*	**700**	*700*	**0.54**	*0.55*	**0.49**	*0.49*	**16**	*17*
Waiwhakaiho	**2112**	*2112*	**853**	*858*	**0.62**	*0.62*	**0.60**	*0.60*	**22**	*22*

A moderately strong positive relationship (correlations: Spearman = 0.54, Pearson = 0.48) between the count of actual VTCI observations and the strength of both correlations exists. More actual observations are associated with stronger correlations. For example, the Kaūpokonui site, with 863 observations, shows high correlations (Spearman = 0.67, Pearson = 0.64). In contrast, Pohokura has lower correlations with only 535 observations (Spearman = 0.44, Pearson = 0.42). There is no statistically significant relationship between the number of 10-day smoothed observations and subsequently observed correlations.

Table 5 summarises correlation and error metrics for each summer period since 2011, using data from all available soil moisture stations (data availability start dates vary by site). Correlations between fast-VTCI and soil moisture fluctuate across summers, peaking in 2019/20 (Spearman = 0.61; Pearson = 0.58) and reaching a low in 2016/17 (Spearman = 0.21; Pearson = 0.22). The 2011/12 summer stands out as a clear outlier in these results. During this period, only three soil-moisture stations (Urutī, Kapoaiaia, and Kaūpokonui) were operating for the full season, with two additional stations (Kōtare and Waiwhakiho) coming online near the end of the summer period. This sparse and uneven spatial coverage likely explains the weaker correlations observed for 2011/12 compared with other years. Site-specific analysis nonetheless shows moderate correlations at the

https://doi.org/10.5194/egusphere-2026-1953
Preprint. Discussion started: 17 July 2026
© Author(s) 2026. CC BY 4.0 License.

established stations during this summer (Spearman correlations between 0.49 and 0.65), while the newly installed Waiwhakiho station exhibited no correlation with fast-VTCI (Spearman = –0.28) until the following summer (2012/13), when its correlations improved markedly (Spearman = 0.71).

Table 5 also presents the equivalent year-wise validation results for the traditional VTCI method. The temporal patterns in correlation strength are broadly consistent with those observed for fast-VTCI, with the highest correlations also recorded in the 2019/20 summer (Spearman = 0.61, Pearson = 0.58) and the weakest during 2016/17 (Spearman = 0.22, Pearson = 0.22). The fast-VTCI results generally return very similar correlation and RMSE values as the traditional VTCI results.

Table 5: Year-wise validation for all sites using both the fast-VTCI (bolded) and traditional VTCI (italics) methods. All results calculated using a SAVI-Polynomial edge set (all p-values <0.01, excluding fast-VTCI 2011/12 where P-values are shown in square brackets).

Period	***n smoothed* observations**		**n VTCI observations**		**Spearman correlation**		**Pearson correlation**		**RMSE (%)**	
2011/12 Summer	**617**	*621*	**181**	*208*	**0.04 [0.37]**	*0.15*	**0.02 [0.64]**	*0.14*	**27**	*26*
2012/13 Summer	**883**	*902*	**326**	*387*	**0.43**	*0.46*	**0.42**	*0.45*	**25**	*24*
2013/14 Summer	**1204**	*1219*	**447**	*492*	**0.34**	*0.35*	**0.35**	*0.37*	**24**	*23*
2014/15 Summer	**1386**	*1402*	**510**	*554*	**0.47**	*0.50*	**0.47**	*0.51*	**25**	*25*
2015/16 Summer	**1456**	*1477*	**497**	*547*	**0.54**	*0.56*	**0.54**	*0.55*	**24**	*23*
2016/17 Summer	**1701**	*1706*	**489**	*517*	**0.21**	*0.22*	**0.22**	*0.22*	**25**	*25*
2017/18 Summer	**1704**	*1718*	**559**	*594*	**0.56**	*0.58*	**0.57**	*0.59*	**20**	*20*
2018/19 Summer	**1759**	*1774*	**654**	*700*	**0.43**	*0.44*	**0.40**	*0.41*	**22**	*22*
2019/20 Summer	**1732**	*1754*	**674**	*712*	**0.61**	*0.61*	**0.58**	*0.58*	**25**	*25*
2020/21 Summer	**1693**	*1705*	**605**	*654*	**0.32**	*0.28*	**0.29**	*0.26*	**23**	*23*
2021/22 Summer	**1560**	*1594*	**606**	*664*	**0.35**	*0.32*	**0.38**	*0.35*	**22**	*22*
2022/23 Summer	**1605**	*1620*	**563**	*603*	**0.28**	*0.27*	**0.28**	*0.29*	**22**	*21*
2023/24 Summer	**1672**	*1716*	**532**	*594*	**0.37**	*0.36*	**0.38**	*0.37*	**27**	*26*

https://doi.org/10.5194/egusphere-2026-1953
Preprint. Discussion started: 17 July 2026
© Author(s) 2026. CC BY 4.0 License.

3.3 Spatial results

The SAVI-Polynomial fast-VTCI edge-index set was used to generate time series maps (Figure 5), which track the evolution and recovery of the 2017/18 drought. Each monthly map presents the mean VTCI between the 10th and 20th day of the relevant month. LCC & DEM filtering means that not all pixels (see fig. 1) have calculated fast-VTCI values.

Figure 5 illustrates the degree to which drought conditions can vary significantly across the region. This variation is particularly evident during the drought's development in November 2017, when coastal areas of the region were most severely affected. The recovery phase, seen in the February and March 2018 maps, shows faster recovery in the inland eastern areas and surrounding the National Park, while the northwestern coastal areas recover more slowly.

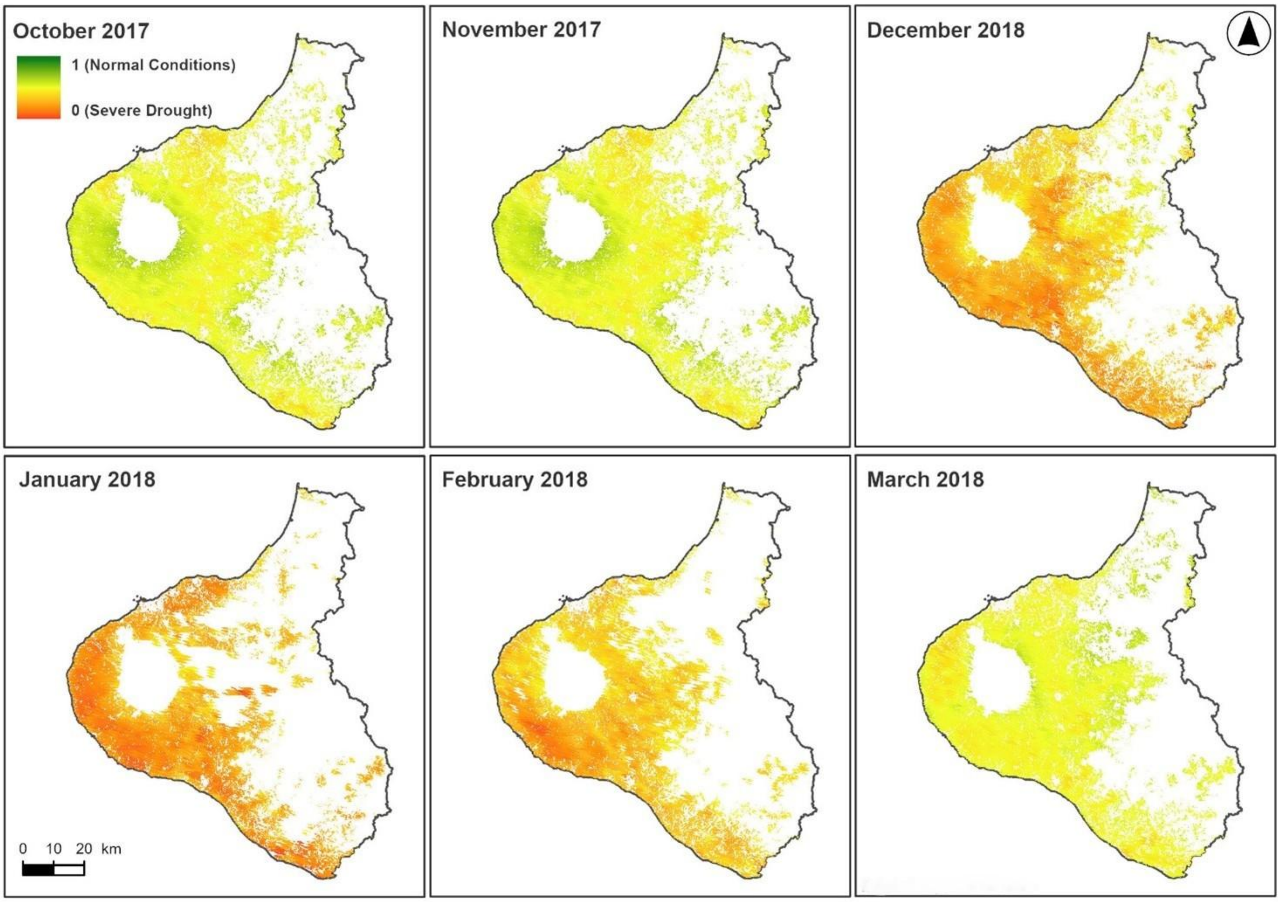

Figure 5: Time series maps for the 2017/18 summer period that track the evolution and recovery from the 2017/2018 drought. We see a sudden intensification of drought conditions in December, this intense drought then persists through January, with recovery starting in February and then approaching pre drought conditions in March.

https://doi.org/10.5194/egusphere-2026-1953
Preprint. Discussion started: 17 July 2026
© Author(s) 2026. CC BY 4.0 License.

3.4 Site-level performance through time

The results of time series drought analysis are presented for the Pātea and Kaūpokonui soil moisture sites. fast-VTCI and traditional VTCI results, both produced using the SAVI-Polynomial edge set, were used to generate these time series. Averaged soil moisture data and normalised and rescaled NZDI are also presented to compare trends across the drought measures. Additional time series charts are included in the supplementary material.

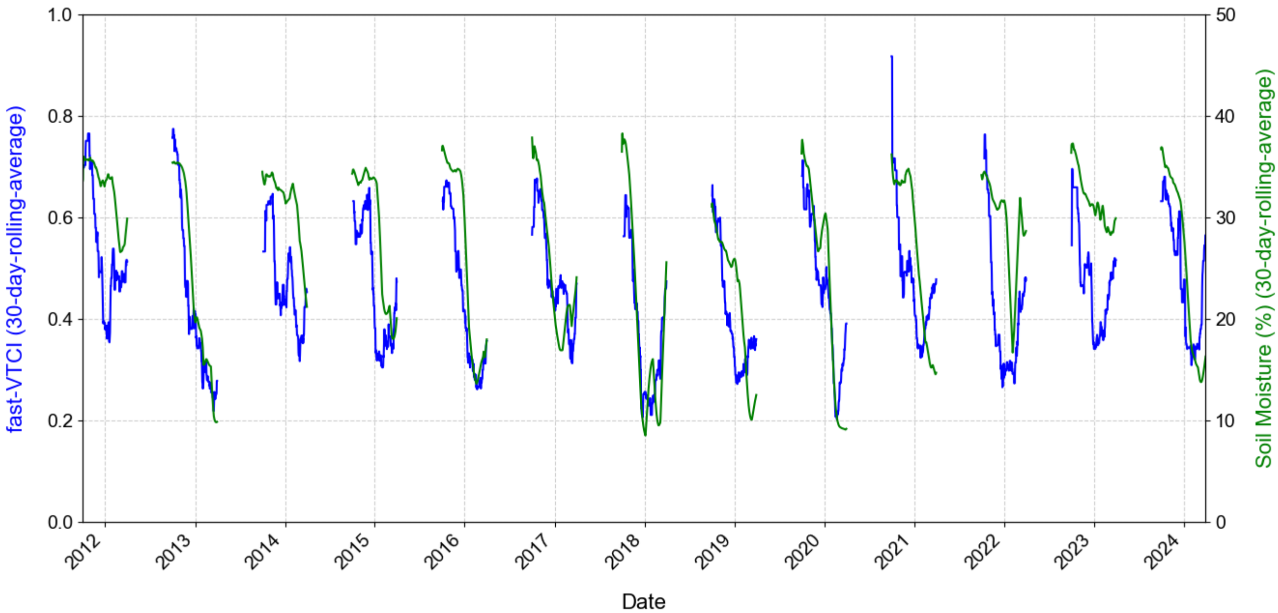

Figure 6: Kaūpokonui site time series for all summer periods since soil moisture records began. fast-VTCI results are shown in blue on a 0 to 1 scale, soil moisture data is shown in green on a 0-45% scale. 30-day rolling averages are applied to both. The traditional VTCI (30-day rolling average) line is visually identical to the fast-VTCI (30-day rolling average) line plotted in this time series.

https://doi.org/10.5194/egusphere-2026-1953
Preprint. Discussion started: 17 July 2026
© Author(s) 2026. CC BY 4.0 License.

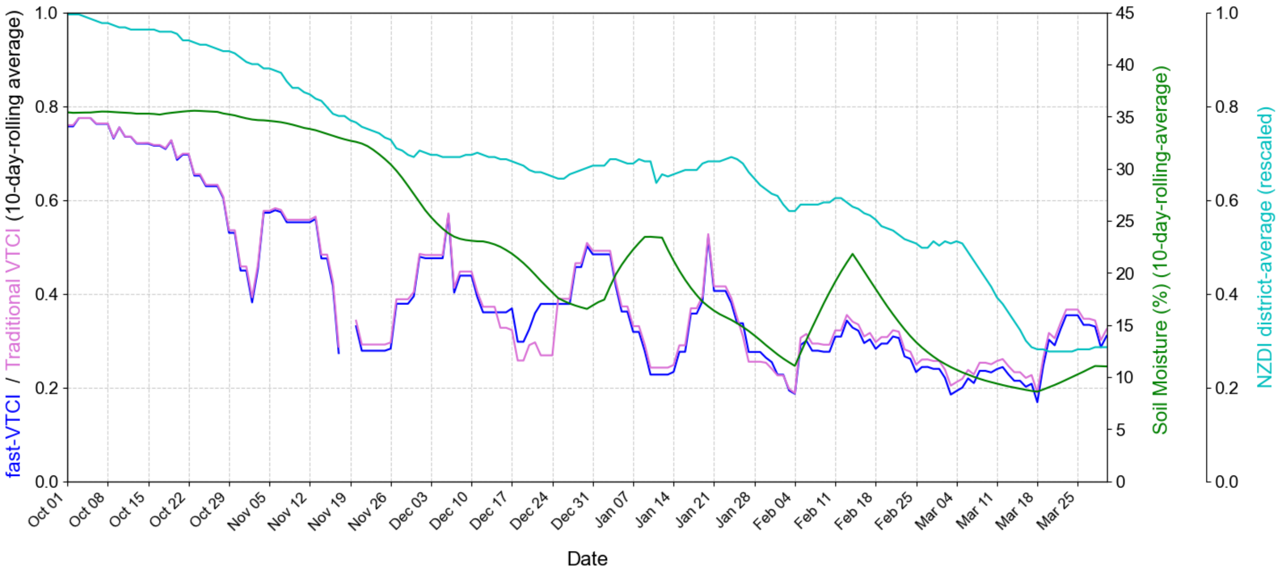

Figure 7: Kaūpokonui site time series for all 2012/13 summer periods with 10-day rolling averages applied to fast-VTCI and soil moisture values. fast-VTCI results are shown in blue and traditional VTCI results are shown in pink on a 0 to 1 scale, soil moisture data is shown in green on a 0-45% scale, and rescaled NZDI district averages are shown in cyan on a 0 to 1 scale.

fast-VTCI results for the Kaūpokonui site demonstrate a seasonal pattern, as shown in Fig. 6. Drought conditions typically develop quickly, reaching their most extreme in the mid-latter part of the summer period before recovering slowly as the summer period concludes. This trend is closely related to the soil moisture trends at the same location. Time series charts for the 2012/13 summer period drought events (Fig. 7) further demonstrate that fast-VTCI results are closely related to soil moisture at the site. NZDI district averages fail to capture some of the variation in soil moisture conditions, which are reflected in the fast-VTCI results. Notably, the traditional VTCI time series follows the fast-VTCI series very closely.

Soil moisture records at the Pātea site began in mid-2016. Since then, fast-VTCI results have shown a good alignment with these records, as seen in Figure 8. The 2017/18 time series (Fig. 9) demonstrates that the NZDI district average poorly represents the soil moisture data available at this site. We examine the NZDI against fast-VTCI in more detail in the discussion. Traditional VTCI results generally track fast-VTCI but appear slightly lower between 11 December 2017 and 1 January 2018. This difference stems from two additional VTCI data points (for 16 and 24 December 2017) being included in the traditional VTCI results but excluded as outliers from the fast-VTCI results as the relevant LST/SAVI values fall outside of the defined edges (see sections 2.3 and 3.2).

https://doi.org/10.5194/egusphere-2026-1953
Preprint. Discussion started: 17 July 2026
© Author(s) 2026. CC BY 4.0 License.

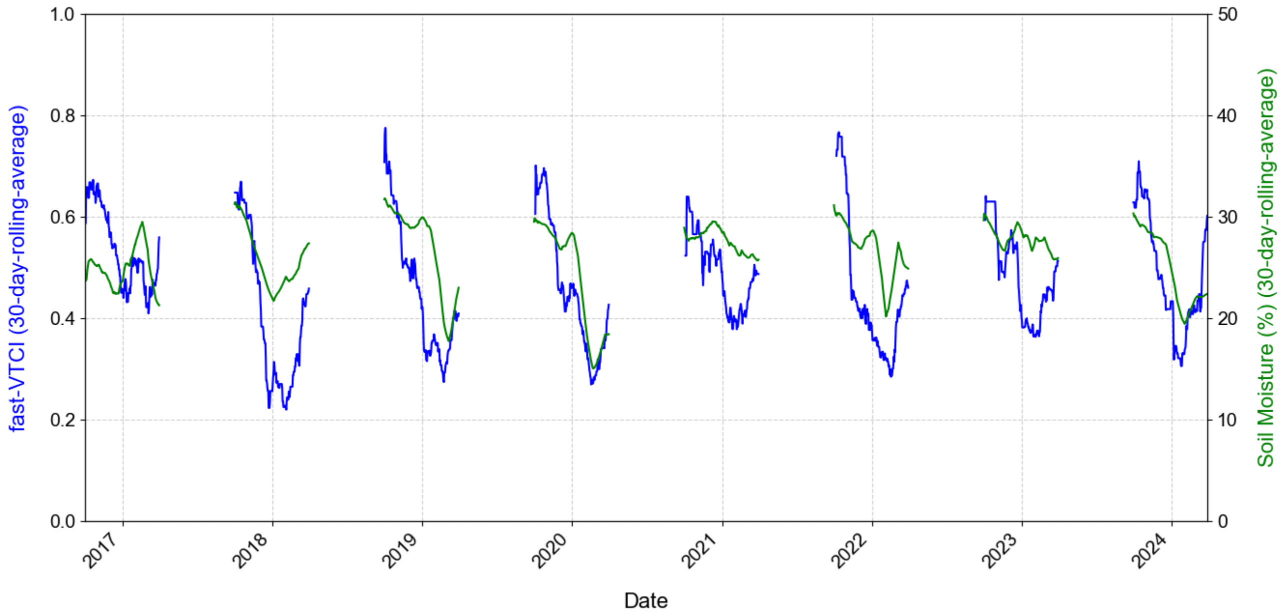

Figure 8: Pātea site time series for all summer periods since soil moisture records began. fast-VTCI results are shown in blue on a 0 to 1 scale, soil moisture data is shown in green on a 0-45% scale. 30-day rolling averages are applied to both. The traditional VTCI (30-day rolling average) line is visually identical to the fast-VTCI (30-day rolling average) line plotted in this time series.

500

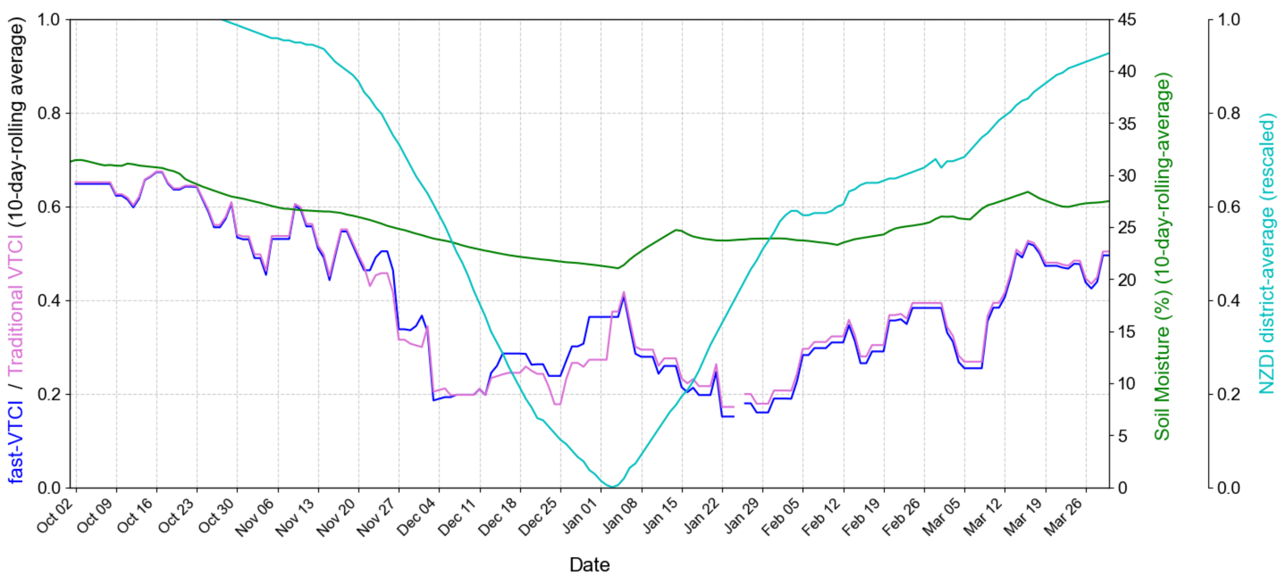

Figure 9: Pātea site time series for 2017/18 summer periods with 10-day rolling averages applied to fast-VTCI and soil moisture values. fast-VTCI results are shown in blue and traditional VTCI results are shown in pink on a 0 to 1 scale, soil moisture data is shown in green on a 0-45% scale, and rescaled NZDI district averages are shown in cyan on a 0 to 1 scale.

https://doi.org/10.5194/egusphere-2026-1953
Preprint. Discussion started: 17 July 2026
© Author(s) 2026. CC BY 4.0 License.

4. Discussion & Limitations

4.1 Vegetation indices and non-linear edge fitting

This study demonstrates notable differences in the LST–VI distributions across NDVI, SAVI, and EVI (see Fig. 10 below), leading to distinct linear and polynomial edge definitions and, consequently, variation in fast-VTCI and validation results. NDVI, though most commonly used in temperature-VI indices, is noted to perform poorly in lush, temperate environments such as New Zealand, where it saturates at moderate pasture densities (Hanna et al., 1999; Wigley et al., 2019). Our results confirm this saturation effect and NDVI's sensitivity to cold soils and dark vegetation, which limit its ability to represent the full spectrum required for robust VTCI calculation in this region.

https://doi.org/10.5194/egusphere-2026-1953
Preprint. Discussion started: 17 July 2026
© Author(s) 2026. CC BY 4.0 License.

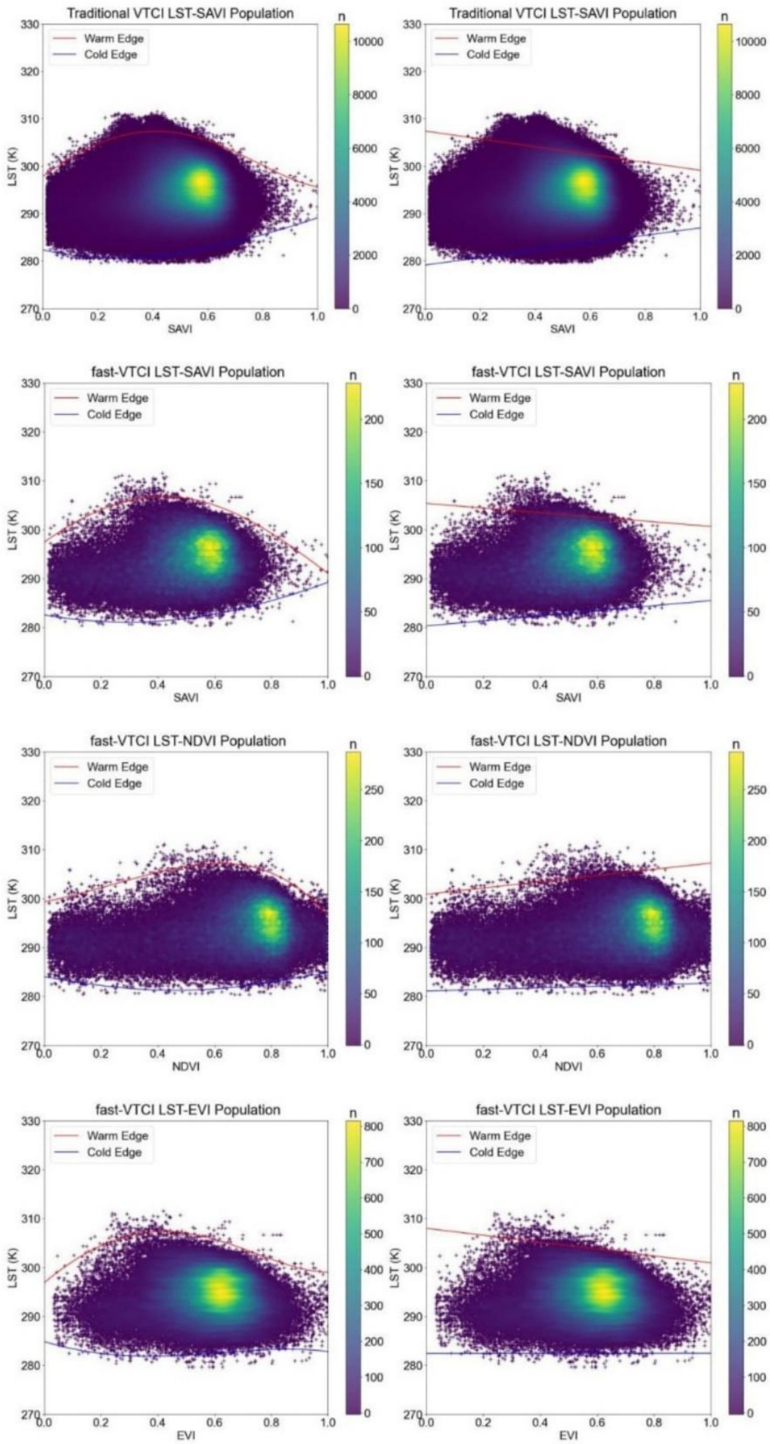

Figure 10: LST-VI Populations built for the Taranaki region using MODIS observations for each summer period since Feb 2000 to March 2024, with both linear and non-linear edges fitted. In the populations, the upper limit (red line) represents the warm edge of the population (LST_{max}), while the lower limit (blue line) represents the cold edge (LST_{min}).

The EVI was designed to correct for soil background effects and exhibits reduced saturation (Huete et al., 2002). Our findings support this, showing less pronounced saturation in the LST–EVI distribution (Fig. 10). Similar to Peng et al. (2016), who found comparable VTCI–soil moisture correlations when testing both EVI and NDVI, our fast-VTCI correlations were broadly consistent across all three VIs tested. Among the three tested indices, the LST–SAVI space most closely resembles the triangular/trapezoidal structure described in the literature (Carlson, 2007; Petropoulos et al., 2009). The SAVI effectively mitigated the observed NDVI saturation effect and achieved the best fit to the observed data. Given Taranaki's characteristically dark and spatially variable volcanic soils (Landcare, n.d.; NZ Soils, n.d.), SAVI's robustness to soil brightness variation further supports its suitability in this study area.

Edge-fitting results demonstrate the superiority of polynomial over linear models in capturing the structure of the LST–VI space across all indices. Polynomial edges produced significantly higher R^2 values, particularly for SAVI (warm and cold edges: 0.88-0.89), exceeding those reported by Liu & Yue (2018) for NDVI, and by Przeździecki & Zawadzki (2023). Polynomial models improved both warm and cold edge representation across all indices, especially SAVI (R^2 = 0.89) and NDVI (R^2 = 0.49), underscoring the limitations of linear edge models. Accurate edge-fitting is critical to the derivation of VTCI. Misspecified upper and lower bounds can significantly distort VTCI values and therefore weaken correlations with in-situ measurements.

4.2 Validation and comparison to previous work

We validated the performance of the newly developed fast-VTCI using in situ soil moisture data from ten sites across the study region, with continuous records spanning up to 13 years, depending on the site. We also conducted the same validation tests using results generated from a traditional VTCI method. While previous studies have assessed VTCI against soil moisture observations, most validation exercises used much shorter timeframes or limited spatial coverage. These differences in validation approaches limit direct comparability. Sun et al. (2008), for instance, evaluated VTCI performance using linear correlations over isolated 10-day windows and reported R-values ranging from -0.075 to 0.757. They concluded that VTCI showed promise as a proxy for soil moisture. Patel et al. (2019) reported R^2 values of 0.54–0.65 when comparing VTCI to soil moisture at three depths (1, 30, and 45 cm) in a semi-arid region. Yu et al. (2018) observed a declining correlation with depth, reporting R^2 values of 0.69 at 0–5 cm, 0.32 at 0–10 cm, and 0.20 at 10–20 cm.

In comparison, we calculated fast-VTCI for all available summer days across the MODIS archive, enabling continuous multi-year validation. Across all sites and years, we observed Pearson correlation coefficients between 0.44 and 0.48 (Table 3), indicating a moderate overall relationship. However, stronger correlations emerged when results were stratified by site and season. For example, at the Pātea site during the 2017/18 summer, correlations exceeded 0.83, surpassing those reported in previous studies.

Unlike the methods used by Sun et al. (2008), Yu et al. (2018), and Patel et al. (2019), which relied on short-term datasets or single-depth measurements, our approach incorporated rolling averages and extensive data records. Soil moisture

https://doi.org/10.5194/egusphere-2026-1953
Preprint. Discussion started: 17 July 2026
© Author(s) 2026. CC BY 4.0 License.

measurements in this study were collected across a 500 mm profile along a 3 m transect on a slope, offering a broad representation of near-surface moisture conditions. Given the depth-dependent weakening of correlation observed by Yu et al. (2018), the comparable or stronger relationships achieved here underscore the robustness of the fast-VTCI approach.

Our validation tests leveraged thousands of joined observations per site (e.g., 1,420 days at Pātea), far exceeding the ~12-31 data points used in earlier studies, providing a more rigorous performance assessment. The same validation steps were applied to the traditional VTCI results generated in this work; comparing the two indices validation results demonstrates that fast-VTCI performs at least as well as the traditional method.

Overall, despite the expanded scope of our validation, the correlation strengths observed remain within the range reported in the literature. However, our findings highlight important spatial and temporal variation in VTCI–soil moisture relationships, with the index performing best during drought periods and at particular sites.

4.3 Taranaki drought trends

We used time-series analysis to explore drought patterns and compare fast-VTCI results with soil moisture, traditional VTCI results and the NZDI.

Cloud cover remains a major challenge for remote sensing in New Zealand (Belliss, 1984; Ashraf et al., 2010). Despite MODIS's 24-hour revisit, substantial cloud in LST and SR data limited fast-VTCI calculations: at Kaūpokonui, only 863 of 2,458 summer days since January 2011 produced valid values, and approximately 23% of days had no usable LST–VI pairs due to clouds or other filtering. Traditional VTCI was similarly affected, with 873 valid VTCI observations over the same period. This limited and irregular data availability underscores the importance of the smoothing techniques applied, which reduced noise and helped produce an improved representation of drought events. The backward-looking rolling averages (10 and 30 day) used for both VTCI and soil moisture introduce a small apparent lead (~5 days) of fast-VTCI relative to soil moisture, as each smoothed value averages the current and preceding days, accentuating VTCI variations relative to the slower soil moisture response. Significantly, data gaps over the smoothing window further contribute to the observed lead of peaks and troughs in the smoothed fast-VTCI signal.

NZDI data indicate that the Taranaki region experienced drought conditions during the 2012/13, 2013/14, 2014/15, 2015/16, 2017/18, 2018/19, and 2019/20 summers (NIWA, 2026). The enhanced spatial resolution of our fast-VTCI results suggests agricultural drought patterns vary across the region. At the Kaūpokonui site, agricultural drought events are also evident in 2016/17 based on the fast-VTCI results. At the Patea site, additional drought events also occurred in 2021/22 and 2023/24.

4.4 fast-VTCI vs Traditional VTCI

We evaluated fast-VTCI and a traditional VTCI correlations with soil moisture across site, year and index-edge combinations. Correlations and RMSE values reported in Tables 3–5 show that fast-VTCI reproduces traditional VTCI performance across the majority of sites and years.

We also measured the computational performance of both indices, with key metrics presented in Table 6 below.

© Author(s) 2026. CC BY 4.0 License.

Table 6: fast-VTCI vs Traditional VTCI Performance Comparison

Metric	fast-VTCI	Traditional VTCI
Average number of LST-VI pairs added to the LST-VI database per image-set for the study region*	33.31	1,553.15
Total number of LST–VI pairs in database	119,749	5,582,010
LST–VI database size	8 MB	150 MB
Per-scene VTCI runtime (HPC)**	~2 minutes	~22 minutes

** The minimum number of pairs for fast-VTCI for a valid image set is 10, while the average number is substantially higher due to the inclusion of multiple summary statistics and the retention of all coincident LST-VI pairs where identical values occur across multiple pixels.*

*** University of Leicester high-performance computing (HPC) cluster (single node). Each standard compute node of the HPC has a pair of 14-core Intel Xeon Skylake CPUs running at 2.6 GHz, and 128 GB of RAM with approximately 428 GB of local storage available.*

Processing compute usage was measured for fast-VTCI using GEE EECU-seconds. To generate the LST-VI database, 1413 EECU-seconds were used; to calculate VTCI from derived edges, an additional 4242 EECU-seconds were used, bringing the total cloud compute per run to 5,655 EECU-seconds (1.57 EECU-hours).

Overall, these results demonstrate that fast-VTCI substantially reduces data volume, computational cost, and processing time relative to traditional VTCI. Although the significant efficiency gains offered by fast-VTCI are not strictly required to process the index on GEE or HPC clusters using MODIS datasets when limited to a test region, they directly lower cloud compute requirements and speed up per-scene runtimes, enabling rapid testing and adaptation. Critically, these results establish proof-of-concept for what becomes operationally essential when applied to higher resolution datasets and larger monitoring extents. As highlighted earlier, other sensors such as Landsat 7, Sentinel-3, commercial constellations and downscaled/fusion datasets can offer LST data at 20-100 m resolution, which, if used to calculate VTCI, would produce orders of magnitude more LST-VI observations than MODIS for the same spatial extent. To illustrate the scalability challenge, our study region at 1km MODIS resolution generates a maximum of approximately 3800 daily observations post filtering, resulting in a 150 MB database. Processing the same region with 100 m resolution data would generate approximately 380,000 observations, at 20 m resolution approximately 9,500,000 observations would be produced per image set. Under these conditions, a traditional VTCI implementation becomes computationally prohibitive not only by data storage requirements but also by input-output overhead, and computational feasibility. This is particularly the case as for an operational monitoring system to function effectively, outlier removal, edge detection and subsequent VTCI calculation must occur with each new image set using an ever-expanding

https://doi.org/10.5194/egusphere-2026-1953
Preprint. Discussion started: 17 July 2026
© Author(s) 2026. CC BY 4.0 License.

full LST-VI database. Because fast-VTCI compresses the LST-VI population for each image set, its computational cost is decoupled from the pixel volume of the original datasets. This decoupling of computational cost from pixel volume represents the core methodological advance that enables operational deployment at agriculturally relevant spatial scales. Although the database does increase in size with each new image set, the magnitude of this increase is very small, even at regional-national scales. As a result, the method becomes increasingly advantageous for higher resolution, large-scale monitoring, enabling the straightforward operational application of 'triangle-based' drought indices to datasets that would otherwise be much more technically demanding and/or financially prohibitive to process.

4.5 Overall effectiveness of fast-VTCI (and vs NZDI)

High-frequency remote sensing approaches, such as those applied in this study, can help overcome long-standing challenges in drought monitoring by producing timely, accessible, and spatially relevant information. We observe moderate correlations between fast-VTCI results and in-situ soil moisture data after applying smoothing techniques; these correlations tend to be stronger during drought years (e.g. Pātea site 2017/18 summer). Site-specific performance varies considerably (Table 4), indicating the need for further investigation. In particular, inland sites such as Kōtare and Pohokura exhibited weaker correlations. We hypothesise that the presence of forestry interspersed with agricultural land cover within the 1000 m pixel resolution could be a key factor contributing to this variability. Additionally, the accuracy of the land cover classification map in these areas may be suboptimal. Further testing is required to fully explore these potential interactions.

The utility of fast-VTCI becomes more apparent when considering the spatiotemporal perspective. Although the index's accuracy may not always match in-situ soil moisture measurements, it provides comprehensive coverage for agricultural drought monitoring at the pixel scale across the study region. The maps in Fig. 5 highlight distinct local variations in drought conditions, especially when compared with the much larger scale NZDI maps currently made available (e.g. Mol et al., 2017 – Figure 5; NIWA, 2026). fast-VTCI effectively captures the heterogeneous nature of drought, both in severity and recovery. The spatial dataset generated for the Taranaki region in this work creates opportunities for further investigation into how drought dynamics interact with local climate, topography, and local agricultural production.

We normalised and rescaled NZDI values to allow for direct comparison with fast-VTCI. Time series plots show that fast-VTCI tracks local moisture variation similarly to NZDI, despite differences in spatial scale. Notably, in years such as 2012/13, 2013/14, and 2014/15, NZDI showed stronger correlations with soil moisture than fast-VTCI (see Table 7). However, analysis of the RMSE shows that fast-VTCI provides a better fit overall, suggesting that while NZDI captures broader drought trends, fast-VTCI better reflects short-term and local variations.

https://doi.org/10.5194/egusphere-2026-1953
Preprint. Discussion started: 17 July 2026
© Author(s) 2026. CC BY 4.0 License.

Table 7: Daily NZDI soil moisture year-wise correlation testing results for soil moisture sites in Taranaki (all p values <0.01).

Period	Observations	Spearman correlation	Pearson correlation	RMSE (%)
2011/12 Summer	636	0.15	0.10	62
2012/13 Summer	932	0.75	0.72	47
2013/14 Summer	1274	0.61	0.65	54
2014/15 Summer	1456	0.67	0.68	51
2015/16 Summer	1564	0.52	0.52	43
2016/17 Summer	1820	0.35	0.30	63
2017/18 Summer	1800	0.55	0.49	48
2018/19 Summer	1820	0.43	0.46	45
2019/20 Summer	1778	0.66	0.61	52
2020/21 Summer	1820	0.45	0.44	63
2021/22 Summer	1806	0.34	0.27	61
2022/23 Summer	1820	0.26	0.24	66

A key consideration is the spatial mismatch between fast-VTCI and NZDI: fast-VTCI operates at 1000m resolution, while the NZDI values used in this work are aggregated over large districts (>2100 km²), likely contributing to discrepancies. NZDI is also interpolated from different meteorological stations than those used for soil moisture in this research, introducing further complexity to comparisons. Despite these differences, fast-VTCI supports drought monitoring at the district to farm scale, which cannot be achieved practically with in-situ soil moisture networks alone due to cost and logistical constraints. In Taranaki, fast-VTCI extends the utility of existing TRC soil moisture stations by providing broader spatial coverage and historical context, with MODIS data available back to 2000. More broadly, fast-VTCI is particularly valuable in agricultural areas without robust soil moisture networks. It can fill spatial data gaps and support decision-making in areas where ground-based monitoring is limited or inaccessible. Leveraging the Google Earth Engine (GEE) platform, fast-VTCI can be rapidly deployed and scaled, removing the computational and technical barriers typically associated with traditional drought indices like VTCI.

https://doi.org/10.5194/egusphere-2026-1953
Preprint. Discussion started: 17 July 2026
© Author(s) 2026. CC BY 4.0 License.

For operational drought monitoring, fast-VTCI effectively identifies drought onset, persistence, and recovery. The index is most valuable for tracking relative changes rather than absolute conditions. In the future, threshold-based drought classification or locally calibrated relationships could be applied to enhance the index's direct comparability to soil moisture data while preserving the index's computational efficiency.

4.5 Limitations & Further Research

Further work could improve fast-VTCI's performance and end-usability for operational agricultural drought monitoring. For example, additional research could better understand the contributing factors behind the variable temporal and spatial performance observed in this work. A key next step is testing LST-VI correlations in the Taranaki region over a more strictly defined summer period. Since VTCI only functions effectively when LST and VI are negatively correlated (Hu et al., 2019), applying dynamic summer period definitions would likely improve the accuracy of edge fitting and subsequent fast-VTCI results.

As discussed, integrating higher spatial resolution data would help reduce the spatial mismatch between fast-VTCI and in-situ soil moisture observations, as well as support more refined, localised insights. Notably, substantial spatial variation is already evident at the 1000 m resolution used in this study, as shown in Figure 5. At finer spatial scales, the effects of on-farm management practices such as local irrigation schemes and drought-resistant cropping strategies, as well as variations in evapotranspiration and drainage, are likely to become more apparent. However, improved spatial resolution often comes at the cost of lower temporal frequency, increasing the likelihood of data gaps due to cloud cover. In such cases, alternative smoothing or gap-filling approaches may be required to maintain robust drought signal interpretation.

A further limitation of this study is the influence of the MODIS view zenith angle on LST retrievals, which can introduce significant uncertainty (Wang et al., 2023). This may compromise the accuracy of LST-VI relationships and reduce the quality of warm and cold edge fitting. Future work should assess the impact of applying LST normalisation techniques before database construction, such as those proposed by Wang et al. (2023) and Na et al. (2024), to correct for these angular effects and improve the robustness of fast-VTCI results. However, despite angular normalisation efforts, residual anisotropic emission related to BRDF and emissivity variations across land cover types may remain and should be accounted for in uncertainty estimation, which also needs further work in terms of quantifying the uncertainty that is introduced by edge definition methods.

Optimising the local implementation of fast-VTCI could be followed by the development of an operational monitoring system. Broader regional testing across other areas of Aotearoa New Zealand is also recommended in order to investigate topographic effects and their management.

© Author(s) 2026. CC BY 4.0 License.

5. Conclusion

Operational drought monitoring requires methods that balance accuracy with computational feasibility, particularly as spatial resolution increases and coverage expands. This research presents fast-VTCI, an improved index that substantially reduces data storage and processing requirements while maintaining equivalent performance to traditional VTCI. fast-VTCI approximates the LST-VI space using daily summary statistics (extrema, median, and percentile values) that preserve the distributional structure required for accurate warm and cold edge detection. This approach reduces data volume by 95% and processing time by approximately 91%.

In this work, we validated the fast-VTCI drought index in the Taranaki region of New Zealand using GEE and MODIS Terra Daily LST and SR data for summer periods from 2000 to 2023. Combining LST-SAVI population approximation with non-linear edge finding yielded moderate to strong correlations with soil moisture (Pearson's $r = 0.44$-0.88, $p < 0.01$), with performance varying spatially and temporally. Critically, the correlations observed using fast-VTCI closely match those achieved using traditional VTCI, demonstrating that the approximation preserves accuracy with respect to tracking soil moisture while reducing computational demands. The method captures substantial within-region variation in drought conditions, offering decision-makers sufficient information to target local interventions.

The statistical approximation applied in this work is transferable to all LST-VI triangle-based methods. Where traditional LST-VI index implementations become computationally prohibitive when applied to emerging higher-resolution thermal sensors, large processing extents or when constrained by cost/processing units, fast-VTCI maintains manageable computational requirements while preserving accuracy. Combined with non-linear edge detection, fast-VTCI enables detailed and timely drought monitoring that can support decision-making across agricultural and water management sectors.

Code and Data Availability

The soil moisture data used in this work can be accessed directly from the Taranaki Regional Council Environmental data hub (TRC, 2026). The NZDI data used can be accessed via NIWA's website (NIWA, 2026). Other datasets used for filtering and index calculation were sourced from the Earth Engine Data Catalog as described in section 2.2. Full code and resulting datasets (including full validation workbooks and all time-series charts) can be accessed on Zenodo using this link: https://doi.org/10.5281/zenodo.19463240 (Smith & Dowling, 2026)

Author contributions

TD: created the fast element of fast-VTCI, wrote the first draft of the original paper, provided supervision and editing since, and acquired the funding to support D. Smith's writing.

DS: conducted the New Zealand validation of fast-VTCI, converted the experimental code to Earth Engine and has led the writing of subsequent versions.

DG: led the original science team, gained the Newton funding for the first version of the work and has contributed to the manuscript.

KV: conducted the initial literature review for the project, assisted with MODIS data handling for initial experimentation and has contributed to the manuscript.

Acknowledgements

We would like to acknowledge the Taranaki Regional Council, especially Dr Jeremy Wilkinson and Andrew Whiteford, who provided the soil moisture data used in this research. We would also like to acknowledge NIWA for use of their NZDI data, which was downloaded and used in accordance with their CC BY-NC 4.0 license. Earlier work conducted on fast-VTCI used the ALICE High Performance Computing Facility at the University of Leicester and STFC JASMIN. This earlier work was supported by E.M.A. Dodd and M. Perry of the National Centre for Earth Observation, Department of Physics and Astronomy, University of Leicester, Leicester, UK. We also thank the reviewers whose comments and work made this paper substantially stronger and better presented.

Financial support

Early work on this project was financially supported by the UKChina Research & Innovation Partnership Fund through the Met Office Climate Science for Service Partnership (CSSP) China as part of the Department for Business, Energy & Industrial Strategy (BEIS) Newton Fund. The specific project, called 'VERDANT', was supported through Grant Agreement P107722. Finally, support for this early work was also received from NERC national capability funding to the National Centre for Earth Observation (NCEO) in the UK. More recently, this work has been supported by the School of Environment, University of Auckland, Auckland, New Zealand.

References

Aliyu Kasim, A., Nahum Carlson, T., & Shehu Usman, H. (2020). Limitations in validating derived soil water content from thermal/optical measurements using the simplified triangle method. *Remote Sensing*, *12*(7), 1155. https://doi.org/10.3390/rs12071155

Aquaflex. (n.d.). Aquaflex in Pasture – Installation Notes. Aquaflex. https://www.aquaflex.co.nz/images/Application_technical_notes/AF267-01-_Aquaflex_Pasture_InstallNotes-200217.pdf

Ashraf, S., Brabyn, L., Hicks, B. J., & Collier, K. (2010). Satellite remote sensing for mapping vegetation in New Zealand freshwater environments: A review. *New Zealand Geographer, 66*(1), 33-43. https://doi.org/10.1111/j.1745-7939.2010.01168.x

https://doi.org/10.5194/egusphere-2026-1953
Preprint. Discussion started: 17 July 2026
© Author(s) 2026. CC BY 4.0 License.

Belliss, S. E. (1984). Remote sensing in New Zealand A status report. *International Journal of Remote Sensing, 5*(6), 877-881. https://doi.org/10.1080/01431168408948874

Buchhorn, M., Lesiv, M., Tsendbazar, N., Herold, M., Bertels, L., & Smets, B. (2020). Copernicus global land cover layers—collection 2. *Remote Sensing, 12*(6), 1044. https://doi.org/10.3390/rs12061044

Cai, J., Zhao, W., Ding, T. and Yin, G., (2025). Generation of High-Resolution Surface Soil Moisture over Mountain Areas by Spatially Downscaling Remote Sensing Products Based on Land Surface Temperature–Vegetation Index Feature Space. *Journal of Remote Sensing*, 5, p.0437.

Caloiero, T. (2017). Drought analysis in New Zealand using the standardized precipitation index. *Environmental Earth Sciences, 76*(16). https://doi.org/10.1007/s12665-017-6909-x

Carlson, T. (2007). An overview of the "triangle method" for estimating surface evapotranspiration and soil moisture from satellite imagery. *Sensors, 7*(8), 1612-1629. https://doi.org/10.3390/s7081612

Chappell, P. R. (2014). *The climate and weather of Taranaki.* New Zealand:

DairyNZ. (2020). Average pasture growth data (kg/ DM/ha/day) Taranaki. DairyNZ.

Dowling, T.P.F., Langsdale, M.F., Ermida, S.L., Wooster, M.J., Merbold, L., Leitner, S., Trigo, I.F., Gluecks, I., Main, B., O'Shea, F. and Hook, S., (2022). A new East African satellite data validation station: Performance of the LSA-SAF all-weather land surface temperature product over a savannah biome. ISPRS Journal of Photogrammetry and Remote Sensing, 187, pp.240-258.

Didan, K., & Munoz, A. B. (2019). MODIS Vegetation Index User's Guide (MOD13 *Series).* https://lpdaac.usgs.gov/documents/621/MOD13_User_Guide_V61.pdf

Duan, X., Jahangir, Z., Lu, L., Qazi Muhammad Yasir, Aslam, R. W., Ahmed, R., Naz, I., Muhammad Azeem Liaquat, Jamil, A., & Alzahrani, H. (2025). Enhanced Land-Surface Temperature Recovery Through Multisensor Data Fusion and Spatial Resolution Improvement. *IEEE Journal of Selected Topics in Applied Earth Observations and Remote Sensing*, *18*, 7950–7966. https://doi.org/10.1109/jstars.2025.3548428

Fahrland, E., Paschko, H., Philipp, J., & Kahabka, H. (2022). *Copernicus Digital Elevation Model.* Airbus. https://spacedata.copernicus.eu/documents/20123/121239/GEO1988-CopernicusDEM-SPE-002_ProductHandbook_I4.0.pdf

Ford, T. W., & Quiring, S. M. (2019). Comparison of contemporary in situ, model, and satellite remote sensing soil moisture with a focus on drought monitoring. *Water Resources Research, 55*(2), 15651582. https://doi.org/10.1029/2018WR024039.

GEO: Group on Earth Observations (2025) *GEOGLAM Crop Monitor*, https://www.cropmonitor.org/, accessed 23-09-2025.

https://doi.org/10.5194/egusphere-2026-1953
Preprint. Discussion started: 17 July 2026
© Author(s) 2026. CC BY 4.0 License.

Hanna, M. M., Steyn-Ross, D. A., & Steyn-Ross, M. (1999). Estimating biomass for New Zealand pasture using optical remote sensing techniques. *Geocarto International, 14*(3), 89-94. https://doi.org/10.1080/10106049908542121

Hazaymeh, K., & Hassan, Q. K. (2016). Remote sensing of agricultural drought monitoring: A state of art review. *AIMS Environmental Science, 3*(4), 604-630. https://doi.org/10.3934/environsci.2016.4.604

Hu, X., Ren, H., Tansey, K., Zheng, Y., Ghent, D., Liu, X., & Yan, L. (2019). Agricultural drought monitoring using European Space Agency Sentinel 3A land surface temperature and normalized difference vegetation index imageries. *Agricultural and Forest Meteorology, 279*, 107707. https://doi.org/10.1016/j.agrformet.2019.107707

Hooker, J., Duveiller, G. and Cescatti, A., (2018). A global dataset of air temperature derived from satellite remote sensing and weather stations. Scientific data, 5(1), pp.1-11.

Huete, A., Didan, K., Miura, T., Rodriguez, E. P., Gao, X., & Ferreira, L. G. (2002). Overview of the radiometric and biophysical performance of the MODIS vegetation indices. *Remote Sensing of Environment, 83*(1), 195-213. https://doi.org/10.1016/S0034-4257(02)00096-2

Huete, A. R. (1988). A soil-adjusted vegetation index (SAVI). *Remote Sensing of Environment, 25*(3), 295-309. https://doi.org/10.1016/0034-4257(88)90106-X

Huete, A., Justice, C., & Van Leeuwen, W. (1999). *MODIS vegetation index (MOD13)*. The University of Arizona.

Huete, A.R. and Liu, H.Q., 1994. An error and sensitivity analysis of the atmospheric-and soil-correcting variants of the NDVI for the MODIS-EOS. IEEE Transactions on Geoscience and Remote sensing, 32(4), 897-905. https://doi.org/10.1109/36.298018

Jiang, L., & Islam, S. (1999). A methodology for estimation of surface evapotranspiration over large areas using remote sensing observations. *Geophysical Research Letters*, 26(17), 2773–2776. https://doi.org/10.1029/1999GL006049

Kallis, G. (2008). Droughts. Annual Review of Environment and Resources, 33(1), 85-118. https://doi.org/10.1146/annurev.environ.33.081307.123117

Karnieli, A., Agam, N., Pinker, R. T., Anderson, M., Imhoff, M. L., Gutman, G. G., Panov, N., & Goldberg, A. (2010). Use of NDVI and land surface temperature for drought assessment: Merits and limitations. *Journal of Climate, 23*(3), 618-633. https://doi.org/10.1175/2009JCLI2900.1

KC, B., Chau, H. W., Mohssen, M., Cameron, K., Safa, M., McIndoe, I., Rutter, H., Dark, A., Lee, M., & Pandey, V. P. (2021). Assessment of spatial and temporal variability in soil moisture using multi-length TDR probes to calibrate Aquaflex sensors. *Irrigation Science, 39*, 703-713. https://doi.org/10.1007/s00271-021-00747-x

Khan, J., Wang, P., Xie, Y., Wang, L., & Li, L. (2018). Mapping MODIS LST NDVI imagery for drought monitoring in Punjab Pakistan. *IEEE Access, 6*, 19898-

19911. https://doi.org/10.1109/ACCESS.2018.2821717

Landcare, NZ. (n.d.). *Soils Map Viewer.* Landcare Research. https://soils-maps.landcareresearch.co.nz/ LAWA. (2018). *Land Cover.* https://www.lawa.org.nz/explore-data/land-cover/

Li, M., Wang, P., Tansey, K., Sun, Y., Guo, F., & Zhou, J. (2025). Improved field-scale drought monitoring using MODIS and Sentinel-2 data for vegetation temperature condition index generation through a fusion framework. *Computers and Electronics in Agriculture*, *234*, 110256. https://doi.org/10.1016/j.compag.2025.110256

Liu, Y., & Yue, H. (2018). The temperature vegetation warmness index (TVDI) based on Bi-parabolic NDVITs space and gradient-based structural similarity (GSSIM) for long-term drought assessment across Shaanxi province, China (2000–2016). *Remote Sensing*, *10*(6), 959. https://doi.org/10.3390/rs10060959

Liu, X., Zhu, X., Pan, Y., Li, S., Liu, Y., & Ma, Y. (2016). Agricultural drought monitoring: Progress, challenges, and prospects. Journal of Geographical Sciences, 26, 750-767. https://doi.org/10.1007/s11442-016-1297-9

Ministry for the Environment (MfE). (2024). *Aotearoa New Zealand climate projections.* environment.govt.nz. https://environment.govt.nz/facts-and-science/climatehttps://environment.govt.nz/facts-and-science/climate-change/climate-change-projections/change/climate-change-projections/

Ministry for the Environment (MfE) & Stats NZ. (2020). *Our atmosphere and climate 2020.* New Zealand: Ministry for the Environment & Stats NZ. https://environment.govt.nz/assets/Publications/Files/ourhttps://environment.govt.nz/assets/Publications/Files/our-atmosphere-and-climate-2020.pdfatmosphere-and-climate-2020.pdf

Mol, A., Tait, A., & Macara, G. (2017). An automated drought monitoring system for New Zealand. *Weather and Climate, 37*(1), 23-36. https://doi.org/10.2307/26735444

Moran, M.S., Clarke, T.R., Inoue, Y. and Vidal, A., 1994. Estimating crop water deficit using the relation between surface-air temperature and spectral vegetation index. Remote sensing of environment, 49(3), 246-263. https://doi.org/10.1016/0034-4257(94)90020-5

Muñoz-Sabater, J., Dutra, E., Agustí-Panareda, A., Albergel, C., Arduini, G., Balsamo, G., Boussetta, S., Choulga, M., Harrigan, S., & Hersbach, H. (2021). ERA5-Land: A state-of-the-art global reanalysis dataset for land applications. *Earth System Science Data, 13*(9), 4349-4383. https://doi.org/10.5194/essd-13https://doi.org/10.5194/essd-13-4349-20214349-2021

NIWA. (2026), *New Zealand Drought Monitor.* NIWA. https://niwa.co.nz/hazards/weather-hazards/new-zealand-drought-monitor

NZ Soils. (n.d.). *Soils of NZ: By Region.* New Zealand: NZ Soils. http://www.nzsoils.org.nz/PageFiles/233/SoilsOfNZ%20By%20Region.pdf

FAO: Food and Agriculture Organization of the United Nations (2025) Global Information and Early Warning System on Food and Agriculture (GIEWS), https://www.fao.org/giews/earthobservation, accessed 23-09-2025, Markets and Trade Division (EST), Food and Agriculture Organization of the United Nations (FAO), Viale delle Terme di Caracalla, 00153 Rome, Italy.

Patel, N. R., Parida, B. R., Venus, V., Saha, S. K., & Dadhwal, V. K. (2012). Analysis of agricultural drought using vegetation temperature condition index (VTCI) from Terra/MODIS satellite data. *Environmental Monitoring and Assessment, 184*, 7153-7163. https://doi.org/10.1007/s10661-011-2487-7

Patel, N. R., Mukund, A., & Parida, B. R. (2019). Satellite-derived vegetation temperature condition index to infer root zone soil moisture in semi-arid province of Rajasthan, India. *Geocarto International*, *37*(1), 179–195. https://doi.org/10.1080/10106049.2019.1704074

Peng, J., Loew, A., Zhang, S., Wang, J., & Niesel, J. (2016). Spatial Downscaling of Satellite Soil Moisture Data Using a Vegetation Temperature Condition Index. *IEEE Transactions on Geoscience and Remote Sensing, 54*(1), 558-566. https://doi.org/10.1109/TGRS.2015.2462074

Pedregosa, F., Varoquaux, G., Gramfort, A., Michel, V., Thirion, B., Grisel, O., ... & Duchesnay, É. (2011). Scikit-learn: Machine learning in Python. *the Journal of machine Learning research*, *12*, 2825-2830.

Petropoulos, G., T.N. Carlson, M.J. Wooster, & Islam, S. (2009). A review of Ts/VI remote sensing based methods for the retrieval of land surface energy fluxes and soil surface moisture. *Progress in Physical Geography: Earth and Environment, 33*(2), 224-250. https://doi.org/10.1177/0309133309338997

Plauborg, F., Iversen, B. V., & Lærke, P. E. (2005). In situ comparison of three dielectric soil moisture sensors in drip irrigated sandy soils. *Vadose Zone Journal*, *4*(4), 1037-1047. https://doi.org/10.2136/vzj2004.0138

Price, J. C. (1990). Using spatial context in satellite data to infer regional scale evapotranspiration. *IEEE Transactions on Geoscience and Remote Sensing*, *28*(5), 940–948. https://doi.org/10.1109/36.58983

Przeździecki, K., & Zawadzki, J. (2020). Modification of the land surface temperature – vegetation index triangle method for soil moisture condition estimation by using synop reports. *Ecological Indicators*, *119*, 106823. https://doi.org/10.1016/j.ecolind.2020.106823

Przeździecki, K., Zawadzki, J. J., Urbaniak, M., Ziemblińska, K., & Miatkowski, Z. (2023). Using temporal variability of land surface temperature and normalized vegetation index to estimate soil moisture condition on forest areas by means of remote sensing. *Ecological Indicators*, *148*, 110088. https://doi.org/10.1016/j.ecolind.2023.110088

Przeździecki, K., & Zawadzki, J. (2023). Assessing Moisture Content and Its Mitigating Effect in an Urban Area Using the Land Surface Temperature–Vegetation Index Triangle Method. *Forests*, *14*(3), 578. https://doi.org/10.3390/f14030578

Qi, Y., Huang, B., Zhao, M., Jiang, X., & Mao, W. (2026). Bridging the thermal gap: Generating 10 m, 3-day land surface temperature via Landsat–Sentinel-2 fusion. *Remote Sensing of Environment*, *334*(115227). https://doi.org/10.1016/j.rse.2025.115227

https://doi.org/10.5194/egusphere-2026-1953
Preprint. Discussion started: 17 July 2026
© Author(s) 2026. CC BY 4.0 License.

Rouse, J.W., Hass, R.H., Schell, J.A. and Deering, D.W., (1973). Monitoring vegetation systems in the Great Plains with ERTS, *Proceedings of the Third ERTS Symposium*, Vol. I.

Sandholt, I., Rasmussen, K., & Andersen, J. (2002). A simple interpretation of the surface temperature/vegetation index space for assessment of surface moisture status. *Remote Sensing of environment*, *79*(2-3), 213-224. https://doi.org/10.1016/S0034-4257(01)00274-7

Shi, L., Liu, P., Kloog, I., Lee, M., Kosheleva, A. and Schwartz, J., (2016). Estimating daily air temperature across the Southeastern United States using high-resolution satellite data: A statistical modeling study. Environmental research, 146, pp.51-58.

Smith, D., & Dowling TPF. (2026). EnvironmentalRemoteSensingUOA/fastVTCI-NZ: v1-fastVTCIPeerReview (Beta). Zenodo. https://doi.org/10.5281/zenodo.19463240

StatsNZ (2025) StatsNZ DataFinder, Regional Council 2025 Clipped, https://datafinder.stats.govt.nz/layer/120945-regional-council-2025-clipped/, accessed 10-09-2025.

Sun, W., Wang, P., Zhang, S., Zhu, D., Liu, J., Chen, J., & Yang, H. (2008). Using the vegetation temperature condition index for time series drought occurrence monitoring in the Guanzhong Plain, PR China. International Journal of Remote Sensing, 29(17-18), 5133-5144. https://doi.org/10.1080/01431160802036557

Tang, R., Li, Z., & Tang, B. (2010). An application of the Ts–VI triangle method with enhanced edges determination for evapotranspiration estimation from MODIS data in arid and semi-arid regions: Implementation and validation. *Remote Sensing of Environment, 114*(3), 540-551. https://doi.org/10.1016/j.rse.2009.10.012

Taranaki Regional Council (TRC). (2022). *Our Place Taranaki State of Environment 2022.* Stratford, Taranaki: Taranaki Regional Council. https://www.trc.govt.nz/assets/Documents/Environment/SOE2022/TRC_State-Of-Environment_A4_Web-Spreads.pdf

Taranaki Regional Council (TRC). (2024), *The Taranaki region.* Taranaki Regional Council. https://www.trc.govt.nz/council/council-and-region/the-taranaki-region/

Taranaki Regional Council (TRC). (2026), *Environmental data - Soil moisture.* Taranaki Regional Council. https://www.trc.govt.nz/environment/maps-and-data/regional-overview/

Trnka, M., Kocmánková, E., Balek, J., Eitzinger, J., Ruget, F., Formayer, H., Hlavinka, P., Schaumberger, A., Horáková, V., & Možný, M. (2010). Simple snow cover model for agrometeorological applications. *Agricultural and Forest Meteorology*, *150*(7–8), 1115–1127. https://doi.org/10.1016/j.agrformet.2010.04.012

USGS: United States Geological Survey (2025), Famine Early Warning Systems Network, https://fews.net/about, accessed 23-09-2025.

Vermote, E., & Wolfe, R. (2021). MODIS/Terra surface reflectance daily L2G Global 1km and 500m SIN Grid V061. *NASA EOSDIS Land Processes DAAC.*

Wan, Z., Hook, S., & Hulley, G. (2021). *MODIS/Terra Land Surface Temperature/Emissivity Daily L3 Global 1km SIN Grid V061 [Data set]*. NASA EOSDIS Land Processes Distributed Active Archive Center.

Wan, Z., Wang, P., & Li, X. (2004). Using MODIS land surface temperature and normalized difference vegetation index products for monitoring drought in the southern Great Plains, USA. *International Journal of Remote Sensing, 25*(1), 61-72. https://doi.org/10.1080/0143116031000115328

Wang, P., Xiao-wen Li, Jian-ya Gong, & Song, C. (2001a). Vegetation temperature condition index and its application for drought monitoring. Paper presented at the IGARSS 2001. Scanning the Present and Resolving the Future. *1,* 141-143. https://doi.org/10.1109/IGARSS.2001.976083

Wei, W., Zhang, J., Zhou, L., Xie, B., Zhou, J., & Li, C. (2021). Comparative evaluation of drought indices for monitoring drought based on remote sensing data. *Environmental Science and Pollution Research, 28*, 20408-20425. https://doi.org/10.1007/s11356-020-12120-0

West, H., Quinn, N., & Horswell, M. (2019). Remote sensing for drought monitoring & impact assessment: Progress, past challenges and future opportunities. *Remote Sensing of Environment, 232*, 111291. https://doi.org/10.1016/j.rse.2019.111291

Wigley, K., Owens, J. L., Westerschulte, M., Riding, P., Fourie, J., & Werner, A. (2019). Photogrammetry for assessment of pasture biomass. *Journal of New Zealand Grasslands, 81*(0), 33-40. https://doi.org/10.33584/jnzg.2019.81.394

Wilhite, D. A. (2000). Reducing Societal Vulnerability to Drought: Future Challenges. In D. A. Wilhite (Ed.), *Drought: A Global Assessment*. Routledge.

WikiMedia Commons (2025) https://commons.wikimedia.org/wiki/File:New_Zealand_on_the_globe_(New_Zealand_centered).svg, accessed 10-09-2025.

Yu, H., Li, L., Zhu, W., Piao, D., Cui, G., Kim, M., Jeon, S. W., & Lee, W. (2019). Drought monitoring of the wetland in the Tumen River Basin between 1991 and 2016 using Landsat TM/ETM+. *International Journal of Remote Sensing, 40*(4), 1445-1459. https://doi.org/10.1080/01431161.2018.1524604

Yuan, Y., Ye, X., Liu, T., & Li, X. (2023). Drought monitoring based on temperature vegetation warmness index and its relationship with anthropogenic pressure in a subtropical humid watershed in China. *Ecological Indicators*, *154*, 110584. https://doi.org/10.1016/j.ecolind.2023.110584

Zanaga, D., Van De Kerchove, R., Daems, D., De Keersmaecker, W., Brockmann, C., Kirches, G., Wevers, J., Cartus, O., Santoro, M., Fritz, S., Lesiv, M., Herold, M., Tsendbazar, N.E., Xu, P., Ramoino, F., Arino, O., 2022. ESA WorldCover 10 m (2021) v200. https://doi.org/10.5281/zenodo.7254221

Zhou, X., Wang, P., Tansey, K., Zhang, S., Li, H. and Wang, L., 2020. Developing a fused vegetation temperature condition index for drought monitoring at field scales using Sentinel-2 and MODIS imagery.

https://doi.org/10.5194/egusphere-2026-1953
Preprint. Discussion started: 17 July 2026
© Author(s) 2026. CC BY 4.0 License.

Computers and Electronics in Agriculture, 168, p.105144.

Zhu, W., Shi, X., & Wei, J. (2024). A universal triangle method for evapotranspiration estimation with MODIS products and routine meteorological observations: Algorithm development and global validation. *Agricultural Water Management*, *302*, 109017. https://doi.org/10.1016/j.agwat.2024.109017